Local Atomic and Electronic Structures of Solutes in Hydroxyapatite(Dissertation_全文)

AUTHOR(S):

Murata, Hidenobu

CITATION:

Murata, Hidenobu. Local Atomic and Electronic Structures of Solutes in Hydroxyapatite. 京都大学, 2011, 博士(工学)

ISSUE DATE:

2011-03-23

URL:

https://doi.org/10.14989/doctor.k16038

Local Atomic and Electronic Structures of Solutes in Hydroxyapatite

(ハイドロキシアパタイト中の固溶原子の局所構造と電子状態)

Hidenobu Murata

村田　秀信

2011

Contents

Chapter 1

General Introduction

Materials used for biomedical application have been developed. Various kinds of materials such as metals, ceramics, organic polymers and these composites were used in human body. Requirements of these biomaterials widely ranges: bio-compatibility, mechanical properties and so on. Calcium orthophosphate ceramics is one of the promising biomaterials. A number of calcium orthophosphates based materials were used as alternate bones and teeth [1, 2].

Hydroxyapatite ($Ca_5(PO_4)_3OH$, HAp) is a main inorganic component of human bones and teeth, and thus, it is the most important calcium phosphates. It is well known that synthesized HAp could directly connect bones in human body, and thus HAp ceramics and composite materials containing HAp were widely studied [1-5]. Preparations of HAp were performed by various methods [1, 3] such as the solution-precipitation method, the hydrothermal method and the solid state reaction method. In these methods, experimental conditions were widely varied. This enabled us to control morphologies of HAp. To improve the biological properties of HAp, various kinds of HAp were synthesized. For example, sintered dense ceramics, porous ceramics and granules, and HAp-based composites were used for biomedical applications [4].

Another approach to improve biological properties of HAp was impurity-doping [5]. HAp has two non-equivalent Ca sites, Ca-1 (columnar) site

and Ca-2 (triangular) site, PO_4 site and OH site, as shown in figure 1 and 2. This complicated crystal structure allows various kinds of trace elements to incorporate into HAp crystals. For example, divalent cations such as Mg^{2+}, Sr^{2+}, Ba^{2+}, Zn^{2+}, Cd^{2+} and Pb^{2+} were substituted for Ca-site, SiO_4^{3-}, CO_3^{2-} and AsO_4^{3-} were substituted for PO_4 site and F^-, Cl^-, Br^- and CO_3^{2-} were substituted for OH^- site [1, 5]. It is known that biological HAp in human body contains various kinds of defects, Ca^{2+}-vacancies, OH^--vacancies, excess H^+ and impurities [1, 2]. These defects and impurities were closely related to biological properties of HAp. Therefore, attempts to control the biological properties of HAp by doping have been reported [4]. For example, Sr^{2+} doping changes the solubility of HAp [6]. The activities of osteoblasts, which was the cell related to bone formation, were changed by doping [7]. It was noted that these defects and impurities might be associated with other defects and impurities. Some researchers reported that Zn^{2+}-doped HAp had Ca^{2+}-deficient composition [8, 9].

Local environments of dopants also attracted interest of many researchers. To investigate local environments of these impurities, wide ranges of techniques were applied [1, 5]: Rietveld analyses of x-ray and neutron diffraction, nuclear magnetic resonance (NMR), infrared (IR) and Raman spectroscopy, x-ray absorption spectroscopy (XAS) and so on. From theoretical point of view, defects and impurities in HAp crystals were investigated with first-principles manner [10-16]. For example, defect formation of Ca^{2+}-vacancies [10-12] and some divalent cations [12-16] were reported. In spite of good explanations on chemistry of defects, these calculations were performed at ground state and thus did not consider temperature effect.

The scope of this thesis was revealing the local atomic configurations of solutes in HAp. For this purpose, first-principles calculations and XAS were adopted. This thesis was constituted of following chapters.

In Chapter 2, Zn^{2+}-dopant in Ca^{2+}-deficient HAp crystal was investigated by x-ray absorption spectroscopy (XAS) with aid of first-principles calculations. The XRD patterns of the sample were assigned to HAp and no secondary phase was observed. Experimental XAS spectra were interpreted with first-principles supercell method with a core-hole effect. The experimental Zn-K XAS have different feature from calculated spectra of simple substituted models that Zn^{2+} substituted for Ca-sites. Synthesized sample has Ca^{2+}-deficient composition, and thus the models that Zn^{2+} was associated with Ca^{2+}-vacancy and excess H^{+} were constructed to include the effect of Ca^{2+} vacancies directly. One of these models well reproduced experimental Zn-K XAS spectra. It was found Ca^{2+}-vacancies have an important role for dopants to substitute into HAp.

Chapter 3 treated the effect of Ca^{2+} vacancies to solutes, Mg^{2+}, Sr^{2+}, Ba^{2+}, Zn^{2+}, Cd^{2+} and Pb^{2+}, in HAp. Calculated models were constructed, based on the one that was found in chapter 2. Incorporation with Ca^{2+}-vacancy defect complex enabled solutes and its surrounding atoms to be further optimized. Substitution energies of these solutes were reduced with incorporation with Ca^{2+}-vacancy defect complex except Cd^{2+} and Pb^{2+}, which had low substation energies in perfect HAp model. For other solutes, the absolute difference of ionic radii between Ca^{2+} and solutes were important factor to stabilize.

In Chapter 4, temperature effects of Sr^{2+}-dopants in HAp were discussed on by both experiments and first-principles calculations. Local environments of

Sr^{2+}-doped HAp synthesized different temperature were investigated by XAS. It was found that the amounts of Sr^{2+} substituted for Ca-2 site increased at high temperature while Ca-1 site was preferential site in Sr^{2+}-doped HAp synthesized at room temperature. To reveal the origin of this change, first-principles lattice dynamics calculations for Sr^{2+}-doped HAp were carried out. It was found that phonon effect stabilized Sr^{2+} substituted for Ca-2 site. According to these experimental and calculated results, it was concluded that temperature effects could change substitution site of solutes in HAp.

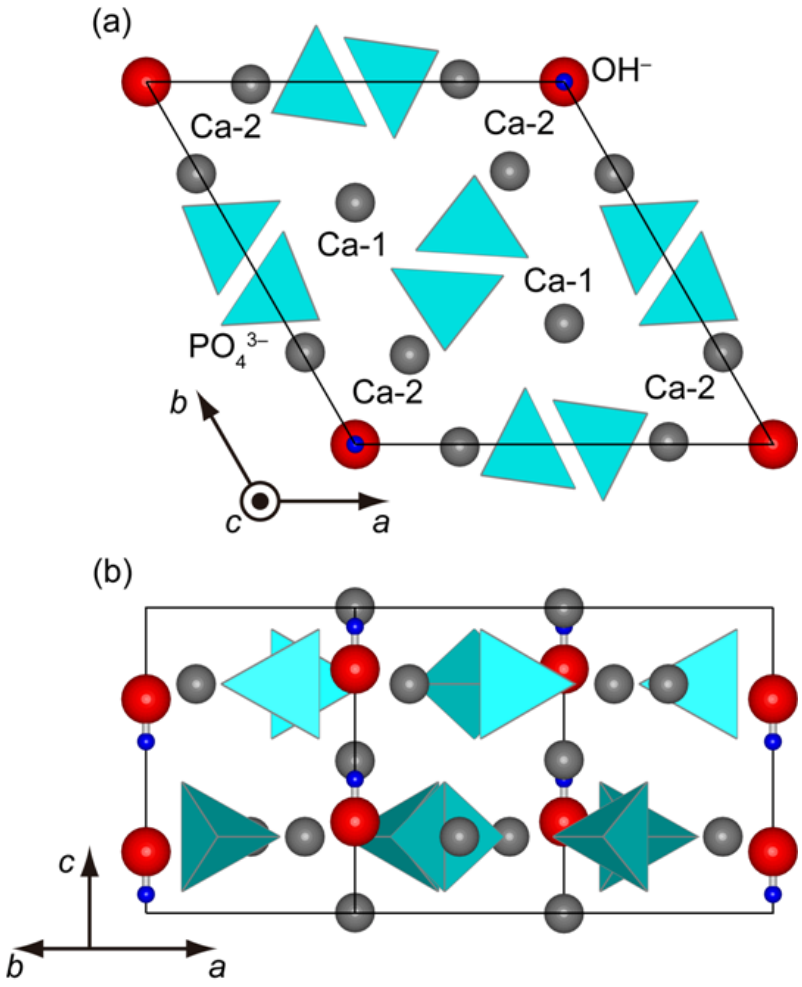

Figure 1 Crystal structure of hexagonal hydroxyapatite (a) viewed along c-axis and (b) viewed along a-b plane. This figure was drawn by VESTA code [16].

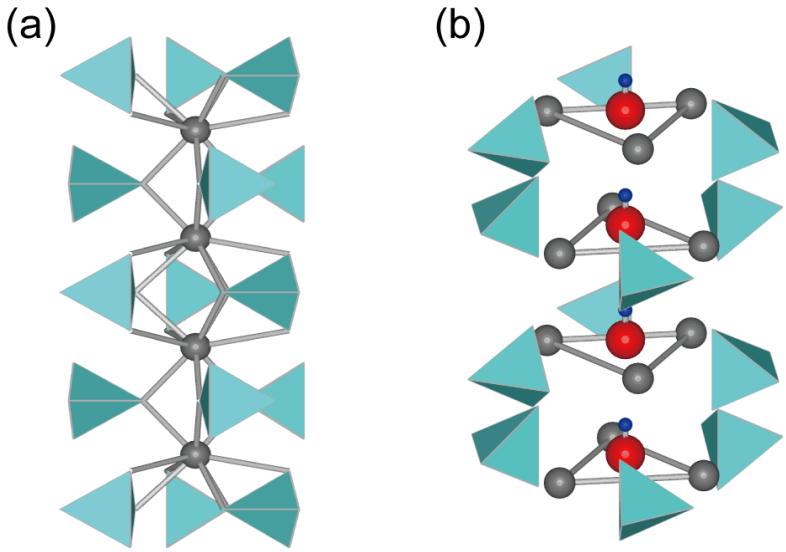

Figure 2 Local environments of (a) Ca-1 (columnar) site and (b) Ca-2 (triangular) site. This figure was drawn by VESTA code [16].

References

[1] J. C. Elliott, Structure and Chemistry of the Apatites and Other Calcium Orthophosphates, Amsterdam, Elsevier, (1994).

[2] S. V. Dorozhkin, J. Mater. Sci. 42, 1061-1095 (2007).

[3] V. P. Orlovskii, V. S. Komlev and S. M. Barinov, Inorg. Mater. 38, 973-984 (2002).

[4] Sergey V. Dorozhkin, J. Mater. Sci. 44, 2343-2387 (2009).

[5] E. Boanini, M. Gazzano and A. Bigi, Acta Biomater. 6, 1882-1894 (2010).

[6] H. B. Pan, Z. Y. Li, W. M. Lam, J. C. Wong, B. W. Darvell, K. D. K. Luk and W. W. Lu, Acta Biomater. 5, 1678-1685 (2009).

[7] T. J. Webster, E. A. Massa-Schlueter, J. L. Smith and E. B. Slamovich, Biomaterials 25, 2111-2121 (2004).

[8] A. Bigi, E. Foresti, M. Gandolfi, M. Gazzano and N. Roveri, J. Inorg. Biochem. 58, 49-58 (1995).

[9] F. Miyaji, Y. Kono and Y. Suyama, Mater. Res. Bull. 40, 209-220 (2005).

[10] K. Matsunaga, Phys. Rev. B 77, 104106 (2008).

[11] D. Zahn and O. Hochrein, J. Solid State Chem. 181, 1712-1816 (2008).

[12] K. Matsunaga, J. Am. Ceram. Soc. 93, 1-14 (2010).

[13] D. E. Ellis, J. Terra, O. Warschkow, M. Jiang, G. B. Gonzalez, J. S. Okasinski, M. J. Bedzyk, A.M. Rossi, and J. G. Eon, Phys. Chem. Chem. Phys. 8, 967-976 (2006).

[14] K. Matsunaga, H. Inamori and H. Murata, Phys. Rev. B 78, 094101 (2008).

[15] J. Terra, E. R. Dourado, J. G. Eon, D. E. Ellis, G. Gonzalezd and A. M. Rossia, Phys. Chem. Chem. Phys. 11, 568-577 (2009)

[16] K. Kawabata and T. Yamamoto, J. Ceram. Soc. Japan 118, 548-549 (2010).

[17] K. Momma and F. Izumi, J. Appl. Cryst. 41, 653-658 (2008).

Chapter 2

Local environment of Zn^{2+} in Ca^{2+} deficient hydroxyapatite

1. Introduction

Hydroxyapatite ($Ca_5(PO_4)_3OH$, HAp) is a main inorganic component of human bones and teeth. HAp in human body is not pure, but contains various kinds of defects and impurities, which affect biological properties of HAp such as solubility and adsorption of organic molecules. Therefore, it is attempted to control the biological properties of HAp by doping in materials development for practical use. A number of dopants have already been investigated [1]. Among these dopants, Zn^{2+} is an important element, because it is one of the essential elements for human body to influence activity of osteoclasts in bone remodeling processes [2]. It is also reported that Zn^{2+} in HAp affects the morphology of HAp particles [3, 4]. To understand the effect of Zn^{2+} dopants and design the biological properties of synthetic HAp by Zn^{2+} doping, it is desired to reveal characteristic atomic and electronic structures of doped Zn^{2+} in HAp.

To date, Zn^{2+} dopant in HAp was investigated by several researchers. The reported solubility limit of Zn^{2+} into HAp varied from a few to 15 mol% [3-5]. In addition, synthesized Zn^{2+}-doped HAp often had the Ca-deficient compositions [3, 5]. On the other hand, the local environment of Zn^{2+} in HAp was reported by Tang et al [6]. They carried out the extended X-ray absorption fine structure (EXAFS)

analyses on the coordination number and bond lengths of Zn^{2+} with the surrounding oxygen, and concluded that Zn^{2+} substitutes for the Ca-2 site (triangular Ca in hexagonal HAp) with a fourfold coordination to oxygen. Our previous calculations also reported that Zn^{2+} favors to substitute at the Ca-2 site, but the ionic-substitution energy is too high for Zn^{2+} to incorporate into HAp with the experimentally observed value of more than a few mol% [7]. Since HAp is often in the Ca deficient state [3, 5], it is likely that the Ca^{2+} vacancies may play an important role for the Zn^{2+} incorporation.

X-ray absorption near edge structure (XANES) is a powerful tool to investigate the local environment of trace elements in materials, and thus has been used for analyses of dopants and impurities in metal oxides and semiconductors [8]. This is the case for HAp, and, for example, Zn-K XANES were measured for synthesized Zn^{2+} doped HAp [6], tooth enamel [9], bones and kidney stones [10]. It is necessary to deeply analyze experimentally observed spectra, in order to reveal the local chemical environment of Zn^{2+} in the HAp samples. However, it is not straightforward to analyze the experimental spectra by fingerprint to make comparison with those of reference materials such as ZnO and $Zn_3(PO_4)_2$ because Zn^{2+} ions in the HAp related materials have a different local environment from the references. For this purpose, theoretical calculations of XANES spectra for dilute Zn^{2+} in the HAp-related systems are desirable.

In this study, the local environment of Zn^{2+} in Ca^{2+}-deficient HAp was investigated based on theoretical and experimental analyses of XANES. To take account of the presence of Ca^{2+} vacancies in HAp, several arrangements of substitutional Zn^{2+} and a Ca^{2+} vacancy in HAp were considered. Theoretical Zn-K

XANES spectra obtained from the models of Zn^{2+} in perfect and Ca^{2+}-deficient HAp were compared with experiment, and the characteristic atomic coordinate of substitutional Zn^{2+} in HAp was discussed.

2. Computational Procedure

Electronic structure calculations were performed with the plane-wave basis projector argument wave (PAW) method [11] implemented in VASP code [12-14]. Calculated models were based on an 88-atoms supercell where the hexagonal HAp unit cell, shown in figure 1, was doubled along the c axis. Details of models were discussed below. A cutoff energy of plane wave basis set was taken at 500 eV. The generalized gradient approximation (GGA) proposed by Perdew, Burke, and Ernzerhof (PBE) [15] for the exchange-correlation functional was used. The *k*-points sampling was performed by using a Γ-centered Monkhorst-Pack 2×2×1 mesh [16]. Atomic positions in the supercell were relaxed until the interatomic forces became less than 0.05 eV/Å. In order to check computational accuracy, test calculations were performed in more severe conditions, 550 eV for a cut-off energy or Γ-centered Monkhorst-Pack 4×4×3 mesh for *k*-points sampling. It was confirmed that the total energy convergence was less than 1.5 meV/atom. The optimized atomic structures were drawn by VESTA code [17].

Calculated models were based on 1×1×2 supercell of hexagonal HAp primitive cell. It was noted that the space group of hexagonal HAp is $P6_3/m$ with half occupancies of OH direction. In this study, two OH directions were assumed, i.e. ordered column (-OH-OH-) model and faced column (-OH-HO-) model. It was found that ordered column model has lower energies, 1.93 eV/unit cell for GGA-PBE than faced column model. Therefore, ordered column model was employed in this study.

Optimized structural parameters of perfect HAp were shown in table 1, which are in good agreement with experiment. It was noted that ordered column

model has lower symmetry because of lack of mirror plane. This affected Ca-1, P, O1 and O2 site. In this model, Ca-1 site were divided into two sites, called Ca-1a and Ca-1b in the present study. On the other hand, *z* coordinates of P, O1 and O2 sites were slightly shifted from 1/4.

For calculation of Zn^{2+}-doped HAp, two models were considered. One is the model that Zn^{2+} simply substituted for Ca-site. In this study, this model was called perfect HAp model. The other was Zn^{2+} substituted for Ca^{2+} with Ca^{2+}-vacancy and excess H^{+}. This model was called Ca^{2+}-deficient HAp model. Figure 2 shows initial position of Ca^{2+}-deficient model. In Ca^{2+}-deficient model, Zn^{2+} substituted for Ca-2 site. There were two configurations, as shown in figure 2.

For Zn-K XANES calculations, the optimized atomic structures for substitutional Zn^{2+} in perfect and Ca^{2+}-deficient HAp by the above PAW calculations were used, and the full-potential augmented plane wave + local orbitals method (WIEN2k code [19]) in this study. A core-hole was directly treated for final state calculations [8]. The dipole transition was considered as the selection rule. The R_{MT} of each element was set to 1.50, 1.50, 1.45, 1.19 and 0.64 for Zn, Ca, P, O and H, respectively. The $R_{MT}K_{MAX}$, the cut-off parameter of the plane wave, was set to 3.5 bohr $Ry^{1/2}$. The exchange-correlation functional and *k*-point mesh were the same conditions as used in the structural optimizations described above. It is noted that calculated transition energies were generally different from experimental ones [8]. To correct this error, calculated Zn-K XANES spectra in the present study were shifted by -42.7 eV, which was estimated from a transition-energy difference of theoretical and experimental Zn-K XANES for the reference materials of ZnO.

It is also noted that thermal vibrations around the defects in HAp were not explicitly taken into account throughout the present theoretical calculations. However, this would be reasonable because experimental XANES measurements were conducted at room temperature and thermal vibrations at the low temperature may not have a strong influence on the local chemical environment around the defects in HAp.

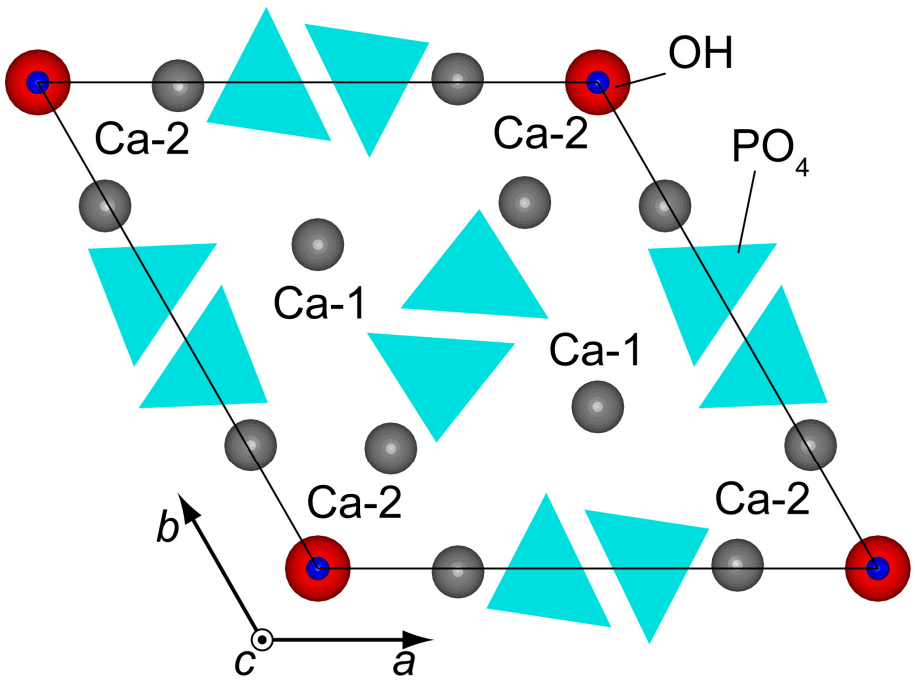

Figure 1 Crystal structure of hexagonal HAp viewed along the *c*-axis

Table 1 Structure parameters of pure HAp

		Present calc.	Expt.[a]
Space Group		$P6_3$	$P6_3$/m
a (Å)		9.566	9.432
c (Å)		6.904	6.881
Ca-1[b]	a	1/3, 2/3, 0.002	1/3, 2/3, 0.0014(4)
	b	1/3, 2/3, 0.499	1/3, 2/3, 0.4986(4)
Ca-2		0.251, 0.000, 0.250	0.2466(2), 0.9931(2), 1/4
P		0.400, 0.369, 0.249	0.3982(2), 0.3682(2), 1/4
O1		0.333, 0.487, 0.248	0.3283(2), 0.4846(2), 1/4
O2		0.588, 0.464, 0.254	0.5876(2), 0.4652(2), 1/4
O3		0.345, 0.260, 0.066	0.3433(1), 0.2579(1), 0.0705(2)
O4		0, 0, 0.216	0, 0, 0.2008(7)
H		0, 0, 0.074	0, 0, 0.0617(15)

[a] reference 18

[b] Because of lack of mirror plane in ordered model, Ca-1 site of hexagonal HAp was divided into two sites, Ca-1a and Ca-1b

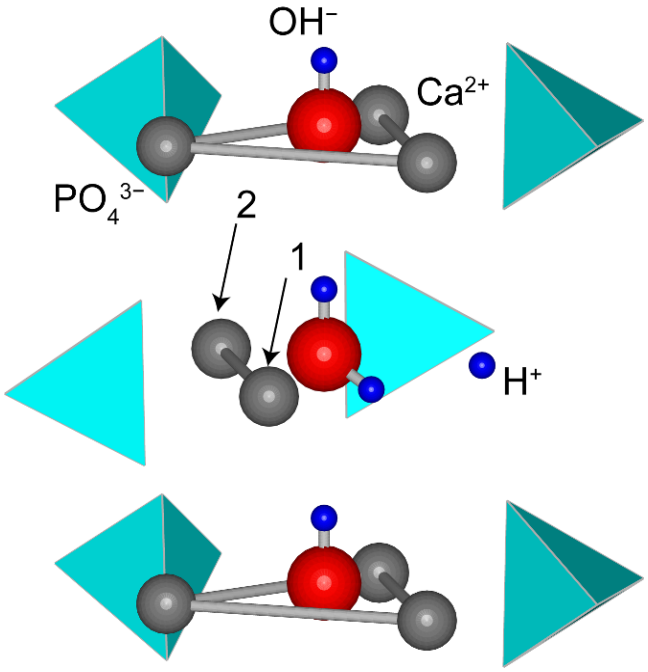

Figure 2 Initial position of Ca^{2+}-deficient HAp

Excess H^+ were lie at the position of Ca^{2+} vacancies. Arrows means Zn^{2+} substitution sites, “1” means model 1 and “2” means model 2.

3. Experimental Procedure

Zn^{2+}-doped HAp (HAp:Zn^{2+}) samples were synthesized by the precipitation method at room temperature. $Ca(NO_3)\bullet 4H_2O$ (Wako pure chemical industries, 99.9%), $Zn(NO_3)_2\bullet 6H_2O$ (Wako pure chemical industries, 99.9%) and $(NH_4)_2HPO_4$ (Wako pure chemical industries, special grade) were used as starting materials. At first, 0.1 mol/L aqueous solutions of the stating materials were prepared. Then, 60 ml of the $(NH_4)_2HPO_4$ solution was dropped into 100 ml of the $Ca(NO_3)_2$ and $Zn(NO_3)_2$ solutions. In this case, the ratio of Ca to Zn was set to 99:1. The solution was mixed with the magnetic stirrer and matured for an hour. During mixing and maturing, the solution pH was kept to 10 with NH_3 aqueous solution. After maturing, the samples were filtrated, washed by distilled water and dried at 323 K for 24 hours.

The obtained samples were characterized with X-ray diffraction (XRD), inductively coupled plasma atomic emission spectroscopy (ICP-AES) and XANES. The XRD patterns were measured with the Bragg-Brentano-type diffractometer (Smart Lab., Rigaku Corporation) using Cu-Kα radiation (40 kV and 30 mA) with the graphite (0002) counter-monochromator. The divergence slit (DS), the scattering slit (SS) and the receiving slit (RS) were set to 1/2°, 1/2°, 0.30 mm, respectively.

Experimental Zn-K XANES spectra were measured by the fluorescent mode with using the Ge 19-element solid state detector at BL01B1 in SPring-8, Japan. In the XANES measurements, X-ray beam was monochromatized with double crystals. For the Zn-K edge (9.65 keV) region, Si-(311) or Si-(111) double crystals are available at BL01B1 in SPring-8, which were both used in the present

study. The Si-(311) double crystals provide smaller beam intensity than Si-(111), whereas gives higher energy resolution.

4. Results and discussion

Figure 3 shows a typical XRD pattern obtained from synthesized HAp:Zn^{2+}. All of the peaks can be assigned to those from HAp, which indicates no secondary phase in the present samples. Its profile was somewhat broad, but it was often found for samples obtained by the similar low temperature process [1]. The chemical composition of the HAp samples measured by ICP was a molar ratio of Zn/(Ca+Zn) = 0.68×10^{-2} and the (Ca+Zn)/P molar ratio of 1.51, which was lower than the stoichiometric composition of (Ca+Zn)/P = 1.67. These values were also lower than the nominal composition of Zn/(Ca+Zn) = 0.01 and (Ca+Zn)/P = 1.67.

Figure 4 shows the experimental Zn-K XANES of HAp:Zn^{2+} using the Si-(111) and Si-(311) double crystal monochromators. The spectrum measured with Si-(311) was sharper than that with Si-(111). There are two prominent peaks marked with A and B and a weak peak marked with C around 9675 eV. The same features were also reported by Tang et al. [6]. In addition, there was a pre-edge peak marked with P, which was clearly observed in the spectrum with Si-(311).

For the XANES calculations of Zn^{2+} dopant in HAp, two situations were considered: isolated Zn^{2+} and Zn^{2+} associated with a Ca^{2+} vacancy. In the former case, since HAp has two Ca sites, Ca-1 (columnar) and Ca-2 (triangular) (see Fig. 1), Zn^{2+} ions substituted for the Ca sites were calculated. Hereafter, these models were called as Zn^{2+} in 'perfect HAp'. For the latter case, several different arrangements of Zn^{2+} and a Ca^{2+} vacancy were considered, which will be discussed again later.

Figure 5 shows a comparison of the experimental Zn-K XANES of synthesized HAp:Zn^{2+} and the calculated ones of Zn^{2+} in perfect HAp. It was noted

that the calculated spectra of Zn^{2+} at Ca-1a and Ca-1b did not have meaningful difference. Therefore, Ca-1a site represented Ca-1 site. The calculated spectra of Zn^{2+} at Ca-1 and Ca-2 exhibited different features from each other. This may be because of the difference in the local environment between the two Ca sites. It was found that Zn^{2+} at Ca-1 has a six-fold coordination with oxygen (the average Zn-O bond length of 2.22 Å) while Zn^{2+} at Ca-2 has the fourfold coordination (the average Zn-O bond length of 2.10 Å). The fourfold coordination is a typical and favorable local chemical environment of Zn in zinc compounds, and it is likely that hybridization of Zn-4*s* and 4*p* orbitals gives rise to the appearance of the pre-edge peak, unlike the case of the six-fold coordination. In order to investigate the pre-edge peak P in more detail, partial densities of states (PDOSs) of Zn and its neighboring O in perfect HAp were also analyzed in figure 6. Since Zn-K XANES is caused by electronic dipole transition from Zn-1*s* to Zn-4*p*, the PDOS profiles correspond to those in the conduction band. A major difference between Ca-1 and Ca-2 substitutions can be seen at the first peak of around 3eV. In the case of the Ca-1 substitution, the peak is mainly composed of the Zn-4*s* component, whereas significantly contains the Zn-4*p* component in the Ca-2 substitution. Therefore, hybridization of 4*s* and 4*p* orbitals of Zn occurs in the fourfold coordination of the Ca-2 substitution, which results in the appearance of the pre-edge peak P in the experimental and theoretical Zn-K XANES.

The theoretical spectra from the substitution models in perfect HAp also showed different spectral features from the experimental one. For example, in the Ca-1 case, the peak positions were different from the experimental one and a shoulder existed around the 9661 eV. On the other hand, the splitting of the peak A

and B in the Ca-2 substitution was narrower and closer to that in experiment than that in the Ca-1 case, and the pre-edge peak around 9658 eV also appeared. However, the peak C was not found in the Ca-2 substitution as well as in the Ca-1 substitution.

Regarding the discrepancy between theory and experiment shown in figure 5, one of the plausible explanations would be Ca deficiency of HAp. As discussed above, our HAp samples were not stoichiometric but exhibited the Ca deficient chemical composition ((Zn+Ca)/P = 1.51 < 1.67). In contrast, the present calculations in figure 5 assumed incorporation of Zn^{2+} into 'perfect' HAp. Since it is likely that Zn^{2+} replaces Ca^{2+} in HAp, the presence of Ca^{2+} vacancies in HAp may affect the local chemical environment around Zn^{2+} and thus the spectral feature of Zn-K XANES.

According to the previous first-principles calculations [20-22], Ca^{2+} vacancies favor the Ca-2 site substitution associated with two interstitial protons for charge compensation. The atomic structure is displayed in figure 6(a). Formation of this kind of the Ca^{2+}-vacancy defect complex is also close to the defect model by Berry, where the chemical composition of Ca^{2+}-deficient HAp was described as $Ca_{10-x}(HPO_4)_x(PO_4)_{6-x}(OH)_{2-x}(H_2O)_x$ [23]. Moreover, recent experimental EXAFS analyses demonstrated preferential occupation of Zn^{2+} at Ca-2 sites of HAp [6]. This was also supported by the first-principles calculations, although the calculations assumed substitution of Zn^{2+} for Ca^{2+} in 'perfect' HAp [7]. Based on the experimental and theoretical results mentioned above, therefore, HAp supercells containing one Ca^{2+}-vacancy complex (totally, 89 atoms involved) were constructed, and a Zn^{2+} was put into the Ca-2 sites surrounding the Ca^{2+}-vacancy

complex.

As there are a number of possible substitutional Ca sites around the Ca^{2+}-vacancy defect complex, two kinds of the substitutional sites were taken into account in the present study. In these models, Zn^{2+} was substituted for the Ca-2 site in the Ca-2 triangle about the OH^- arrangement, in which the Ca^{2+} vacancy is also located (see figures. 6(b) and 6(c)). In the model 1, Zn^{2+} was bonded to the H_2O moiety while not in model 2. In fact, the distances between Zn^{2+} and H_2O in the model 1 and model 2 were 2.08 Å and 3.12 Å, respectively.

From calculations of substitutional Zn^{2+} in the Ca^{2+}-deficient HAp models, it was found that the total energy difference between the two models was about 0.10 eV. According to the computational accuracy of the present study (1.5 meV/atom), the energy difference was not so large, so that it is difficult to conclude the relative stability of the different defect models by the total energy calculations alone. This may be partly because the Ca^{2+}-deficient HAp models contain the complicated Ca^{2+}-vacancy defect complex. In particular, the defect complex involves interstitial protons around the Ca^{2+} vacancy, and then there may be a number of local energy minima for detailed location of the protons.

Owing to the computational difficulty, therefore, it was again attempted to investigate the local environment of Zn^{2+} in Ca^{2+}-deficient HAp, based on comparison of theoretical Zn-K XANES spectra from the different defect models with experiment. Compared with Zn^{2+} substituted in perfect HAp, the Ca^{2+} vacancy changed the feature of the Zn-K XANES, as shown in figure 7. For the case of model 1, the splitting between the peak A and B was wider than that of Zn^{2+} at the Ca-2 site in perfect HAp. It is worth mentioning here that the peak C appeared in

this model. The pre-edge peak P also existed, which was more clearly observed in the calculated spectrum drawn with the thin line (using a smaller FWHM). On the contrary, only the one peak around 9662 eV was observed in the model 2. It was interesting that the peak C did not appear in the model 2.

As stated before, it is noted that a main difference between the model 1 and 2 is the local atomic coordinate around Zn^{2+}. Zn^{2+} in the model 1 is coordinated to oxygen of the H_2O moiety. Therefore, it is considered that the peak C may arise from the interaction of H_2O-Zn^{2+}. The interaction of H_2O-Zn^{2+} also affects the intensity and position of the pre-edge peak P, which is obviously different from the spectrum for the Ca-2 substitution in perfect HAp (see figure 8).

These results indicate that the defect complex of the Ca^{2+} vacancy and two interstitial protons is located adjacent to substitutional Zn^{2+} in HAp. In fact, the association energy between the Ca^{2+}-vacancy complex and substitutional Zn^{2+} was calculated to be 0.07 eV (attractive), which was obtained from a total energy of the associated supercell minus those of the supercells containing the Ca^{2+}-vacancy complex and substitutional Zn^{2+} individually. Since the Ca^{2+}-vacancy complex and substitutional Zn^{2+} are both charge neutral in HAp, the attractive interaction may be attributed to their elastic interaction due to the lattice relaxations around the defects. Such attractive interactions between substitutional Zn^{2+} and Ca^{2+} vacancies in HAp contribute to stabilization of the point defects in HAp. The defective atomic structure of HAp by Zn^{2+} doping may be closely related to crystal instability of Zn^{2+} doped HAp observed experimentally [5].

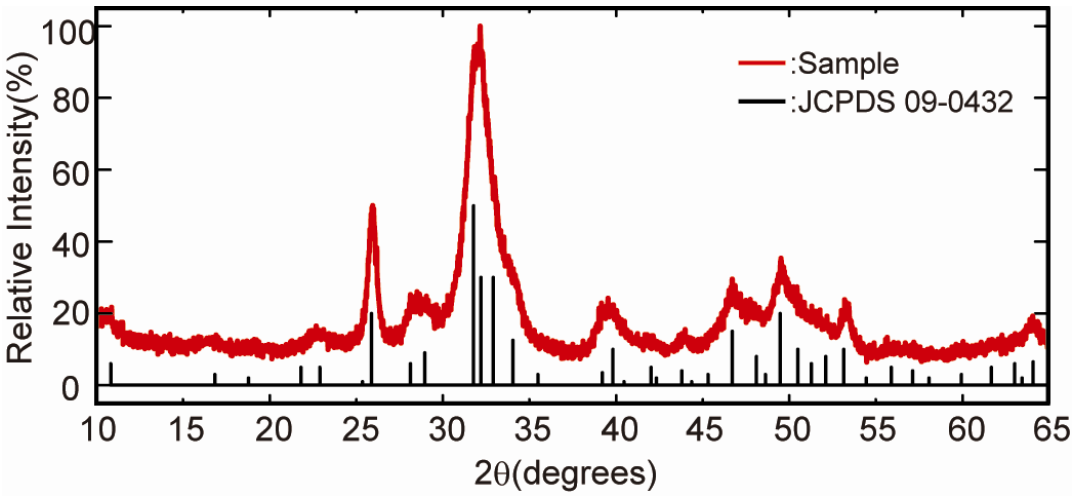

Figure 3 XRD pattern of Zn^{2+}-doped HAp

Red lines were samples and black lines were reference pattern of pure HAp (JCPDS 09-0432)

.

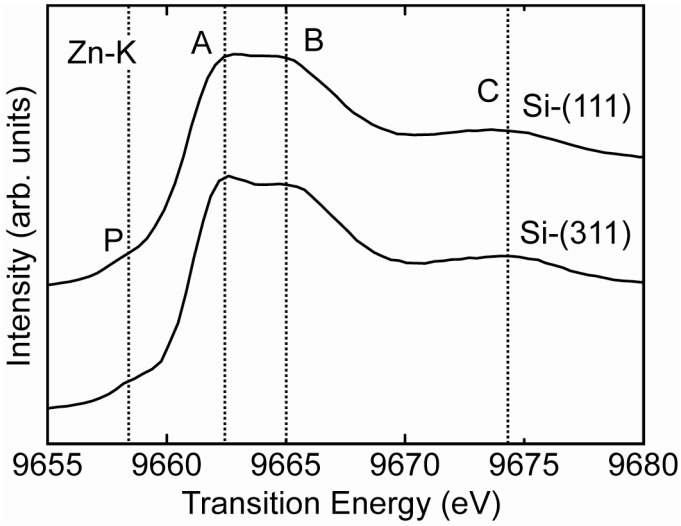

Figure 4 Experimental Zn-K XANES of Zn^{2+}-doped HAp measured with the Si-(311) and Si-(111) double crystal monochromators

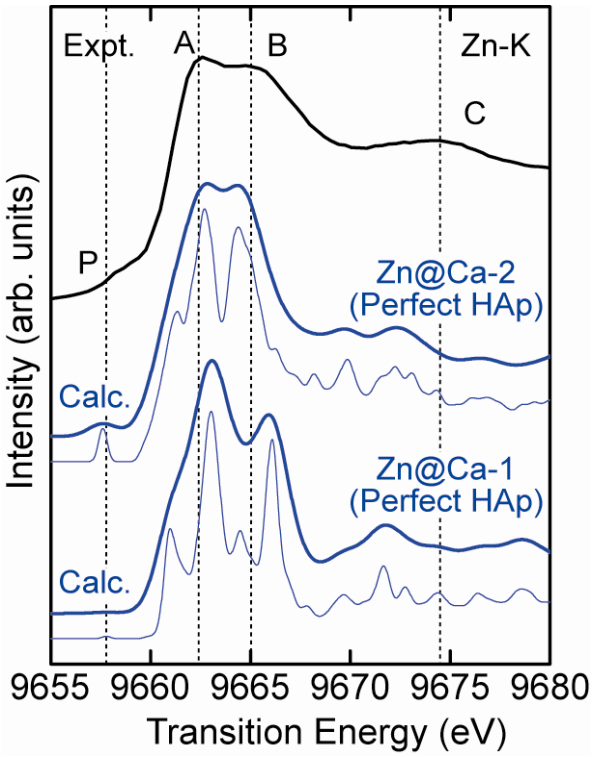

Figure 5 Calculated Zn-K XANES spectra obtained from substitutional Zn^{2+} in perfect HAp. The theoretical spectra were broadened by Gauss functions with two different full widths of half maximum (FWHM) values of 1.67 eV (thick line) and 0.50 eV (thin line).

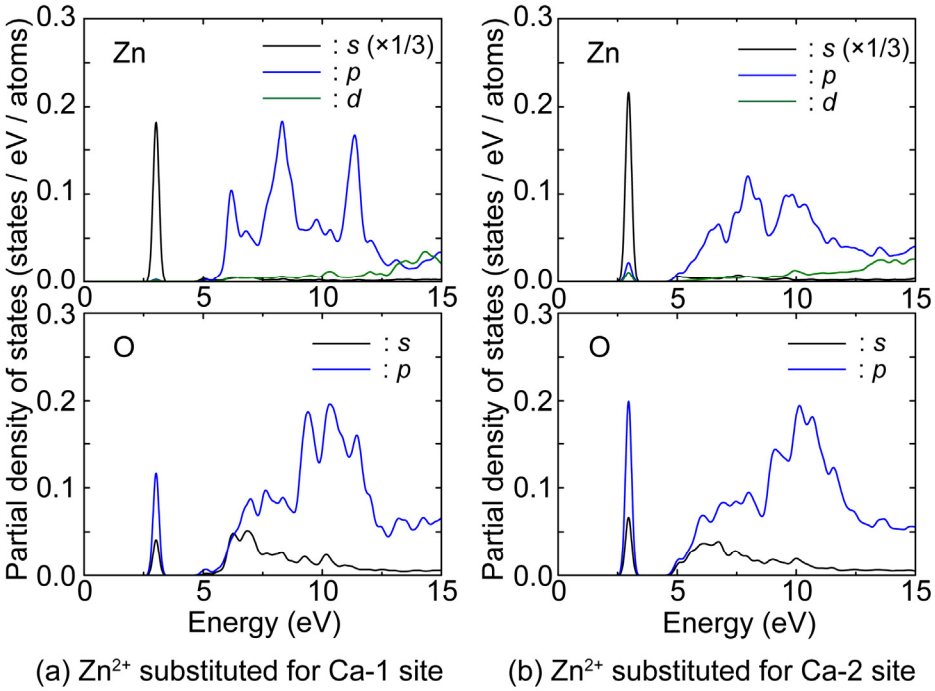

Figure 6 Partial densities of states for Zn and its neighboring O in the final (excited) state: (a) Zn^{2+} substituted for the Ca-1 site and (b) the Ca-2 site of perfect HAp. Zero energies in the profiles were set at the valence band maxima of the HAp supercells.

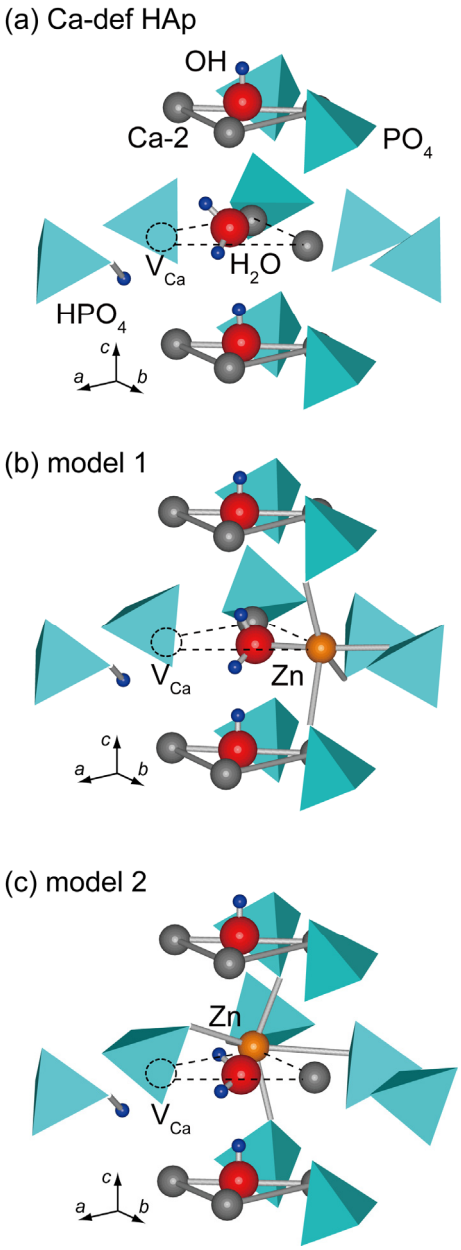

Figure 7. Atomic structures of the Ca^{2+} vacancy defect complex and substitutional Zn^{2+} in HAp. (a) the Ca^{2+} vacancy defect complex, (b) and (c) Zn^{2+} substituted for different Ca-2 sites close to the Ca^{2+} vacancy complex (model 1 and 2)

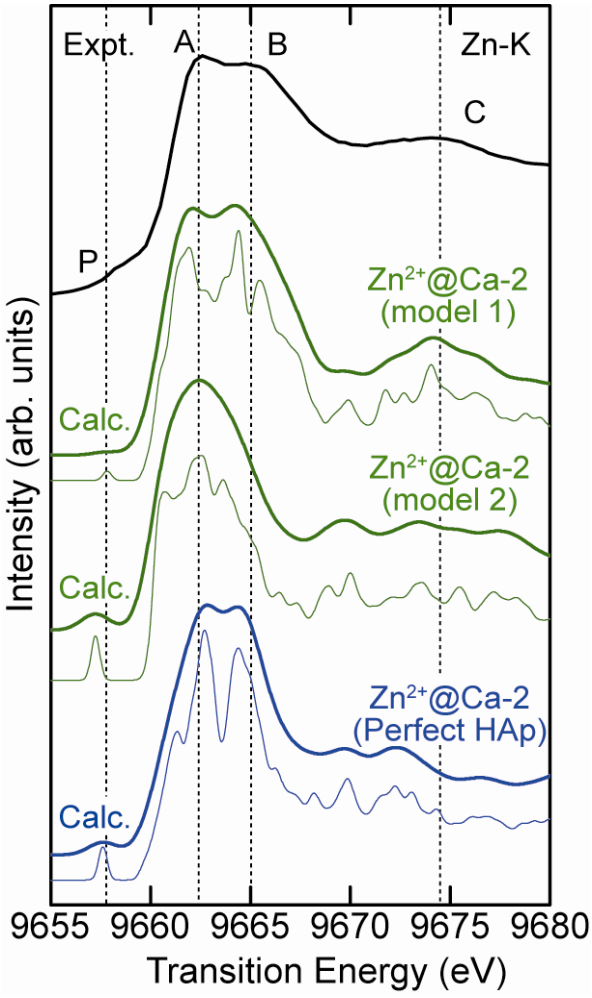

Figure 8. Calculated Zn-K XANES spectra obtained from substitutional Zn^{2+} in Ca-deficient HAp. The theoretical spectra were broadened by Gauss functions with two different FWHM values in the similar way to figure 4.

5. Summary

The local environment of substitutional Zn^{2+} in Ca^{2+}-deficient HAp was investigated using the theoretical and experimental analyses of Zn-K XANES. In the synthesized HAp:Zn^{2+} samples with Zn/(Zn+Ca) = 0.68×10^{-2} by the solution-precipitation method, no secondary phase was observed by XRD.

For the Zn-K XANES calculations, two cases were considered. One was Zn^{2+} substituted for Ca sites in perfect HAp. The other was Zn^{2+} associated with the Ca^{2+} vacancy charge-compensated by two protons. Several arrangements of Zn^{2+} and the Ca^{2+} vacancy defect complex were considered. Ca^{2+} vacancy affected the spectra of Zn^{2+} in Ca^{2+}-deficient HAp. As compared with the theoretical spectra obtained from substitutional Zn^{2+} in perfect HAp, the Ca^{2+}-deficient HAp model for Zn^{2+} at the Ca-2 site coordinated with H_2O showed better agreement with the experimental spectrum. This indicates that the presence of Ca^{2+} vacancies in HAp is important for considering the local atomic structure and stability of substitutional Zn^{2+} in HAp.

References

[1] E. Baonini, M. Gazzano and A. Bigi, Acta Biomater. 6, 1882-1894 (2010).

[2] B. S. Moonga and D. W. Dempster, J. Bone Miner. Res 10, 453-457 (1995).

[3] F. Miyaji, Y. Kono and Y. Suyama, Mater. Res. Bull. 40, 209-220 (2005).

[4] F. Ren, R. Xin, X. Ge and Y. Leng, Acta Biomater. 5, 3141-3149 (2009).

[5] A. Bigi, E. Foresti, M. Gandolfi, M. Gazzano and N. Roveri, J. Inorg. Biochem. 58, 49-58 (1995).

[6] Y. Tang, H. F. Chappell, M. T. Dove, R. J. Reeder and Y. J. Lee, Biomaterials 30, 2864-2872 (2009).

[7] K. Matsunaga, H. Inamori and H. Murata, Phys. Rev. B 78 094101 (2008).

[8] I. Tanaka and T. Mizoguchi, J. Phys.: Condens. Matter 21 104201 (2009).

[9] T. Takatsuka, J. Hirano, H. Matsumoto and T. Honma, Eur. J. Oral Sci. 113, 180-183 (2005).

[10] D. Bazin, X. Carpentier, I. Brocheriou, P. Dorfmuller, S. Aubert, C. Chappard, D. Thiaudière, S. Reguer, G. Waychunas, P. Jungers and M. Daudon, Biochimie 91, 1294-1300 (2009).

[11] P. E. Blöchl, Phys. Rev. B 50 17953 (1994).

[12] G. Kresse and J. Furthmüller, Phys. Rev. B 54, 11169 (1996).

[13] G. Kresse and J. Furthmüller, Comput. Mater. Sci. 6 15 (1996).

[14] G. Kresse G and D. Joubert, Phys. Rev. B 59, 1758 (1999).

[15] J. P. Perdew, K. Burke and M. Ernzerhof, Phys. Rev. Lett. 77, 3865 (1996).

[16] H. J. Monkhorst and J. D. Pack, Phys. Rev. B 13, 5188 (1976).

[17] K. Momma and F. Izumi, J. Appl. Cryst. 41, 653-658 (2008).

[18] M. I. Kay, R. A. Young and A. S Posner, Nature 204 1050-1052 (1964).

[19] P. Blaha, K. Schwarz, G. Madsen, D. Kvasicka and J. Luitz, WIEN2k, an augmented plane wave + local orbitals program for calculating crystal properties. Techn. Universitat Wien, Austria; ISBN: 3-9501031-1-2 (2001).

[20] K. Matsunaga, Phys. Rev. B 77, 104106 (2008).

[21] K. Matsunaga, J. Am. Ceram. Soc. 93, 1 (2010).

[22] D. Zahn and O. Hochrein, J. Sol. State Chem. 181, 1712 (2008).

[23] E. E. Berry, J. Inorg. Nucl. Chem. 29, 317 (1967).

Chapter 3

Effects of Ca^{2+}-vacancies to dopants substitute into HAp

1. Introduction

Hydroxyapatite is a main inorganic component of human bones and teeth. It has a good bio-compatibility and thus promising material to alternate them. HAp in human body has various kinds of defects and impurities. They affect biological properties of HAp. Therefore, it is important to investigate electronic and atomic structure around defects and impurities.

HAp often had Ca^{2+}-deficient composition. In human body, Ca^{2+}-deficient HAp were contained by bones, dentines and enamels [1]. Ca^{2+} vacancies also affect properties of HAp. For example, Ca^{2+}-deficient HAp has higher solubility than stoichiometric HAp and promotes bone formation [2]. As discussed at previous chapter, Ca^{2+}-vacancies were associated with Zn^{2+} dopants. Therefore, it is possible for other impurities in HAp to be associated with Ca^{2+}-vacancies.

From theoretical point of view, various kinds of defects, such as Ca^{2+}-vacancies and impurities, were investigated with first-principles manner [3-9]. It was reported that Ca^{2+} vacancies were associated with excess H^{+} [4, 5]. Substitution energies of divalent dopants were calculated from first-principles calculation and thermodynamics data [6]. It was interesting that Ca-1 site was preferential site for large ions that have larger ionic radii than Ca^{2+} while Ca-2 site

was preferential site for small ions.

In this chapter, local atomic and electronic structures of divalent cations, Mg^{2+}, Sr^{2+}, Ba^{2+}, Zn^{2+}, Cd^{2+} and Pb^{2+} in Ca^{2+}-deficient HAp were investigated by first-principles calculations. Ca^{2+}-vacancy stabilized divalent dopants except Pb^{2+} and Cd^{2+}. It was found that substitution energies were depending on difference of ionic radii.

2. Computational procedures

Electronic and atomic structures were calculated by projector augmented wave (PAW) method [10] implemented by VASP (Vienna Ab-initio Simulation Package) [11-13]. Cut-off energy of plane waves was set to 500 eV. Calculated models were constructed based on 2×2×2 supercell of hexagonal HAp. The sampling of reciprocal space was performed at Γ-point. Exchange-correlation functional were evaluated generalized gradient approximation (GGA) proposed by Perdew, Burke and Ernzerhof [14]. Internal coordinates of atoms were fully relaxed until residual forces became less than 0.02 eV/atom. Under these conditions, energy convergence test were performed with more severe conditions, 550 eV for cut-off energy and Γ-centered Monkhorst-Pack 2×2×2 mesh [15] for *k*-points sampling. It was confirmed that energy convergence were achieved to less than 1.5 meV/atoms. Calculated models were visualized by VESTA code [16].

In the present study, calculated models were divided into two models: M^{2+} simply substituted for Ca site, called perfect HAp model and M^{2+} substituted for Ca site with Ca^{2+}-vacancy and excess H^{+}, called Ca^{2+}-deficient HAp model. Figure 1 shows initial position of Ca^{2+}-deficient HAp model.

For calculation of ionic substitution energies, chemical reactions of divalent cations M^{2+} were substituted for HAp with Ca^{2+}-vacancies. These reactions were represented by

$$Ca_5(PO_4)_3OH + xM^{2+} + 2yH^{+} \rightleftarrows Ca_{5-x-y}M_x(PO_4)_3OH + (x+y)\ Ca^{2+}$$

For perfect HAp model, there were no Ca^{2+} vacancies and thus y equals 0. In our Ca^{2+}-deficient models, the numbers of M^{2+} and Ca^{2+}-vacancies were the same.

Ionic substitution energies of divalent dopants E_{sub} were defined by

difference of free energy:

$$E_{sub} = G_{\mathrm{HAp:M^{2+},V_{Ca^{2+}}}} - G_{\mathrm{HAp}} + (x+y)\mu_{\mathrm{Ca^{2+}}} - x\mu_{\mathrm{M^{2+}}} - 2y\mu_{\mathrm{H^{+}}} \quad (1)$$

where $G_{\mathrm{HAp:M^{2+},V_{Ca^{2+}}}}$ and G_{HAp} were free energies of HAp including M^{2+} and Ca^{2+} vacancies and pure HAp, respectively. If temperature dependence of these terms were neglected, they were the total energies calculated by first-principles calculations. Other terms, $\mu_{\mathrm{Ca^{2+}}}$, $\mu_{\mathrm{M^{2+}}}$ and $\mu_{\mathrm{H^{+}}}$ were chemical potential of Ca^{2+}, M^{2+} and H^{+}, respectively. The chemical potential term could be expanded using thermodynamic relations, i.e.

$$(x+y)\mu_{\mathrm{Ca^{2+}}} - x\mu_{\mathrm{M^{2+}}} - 2y\mu_{\mathrm{H^{+}}}$$

$$= (x+y)\mu^{0}_{\mathrm{Ca^{2+}}} - x\mu^{0}_{\mathrm{M^{2+}}} - 2y\mu^{0}_{\mathrm{H^{+}}} + k_{\mathrm{B}}T\ln\frac{a^{x+y}_{\mathrm{Ca^{2+}}}}{a^{x}_{\mathrm{M^{2+}}}a^{2y}_{\mathrm{H^{+}}}} \quad (2)$$

$\mu^{0}_{\mathrm{Ca^{2+}}}$, $\mu^{0}_{\mathrm{M^{2+}}}$ and $\mu^{0}_{\mathrm{H^{+}}}$ were standard chemical potentials of Ca^{2+}, M^{2+} and H^{+}, respectively. k_{B} is a Boltzmann's constant. The chemical potential terms were further expanded:

$$(x+y)\mu^{0}_{\mathrm{Ca^{2+}}} - x\mu^{0}_{\mathrm{M^{2+}}} - 2y\mu^{0}_{\mathrm{H^{+}}}$$

$$= (x+y)\Delta G^{0}_{f}(\mathrm{Ca^{2+}}) - x\Delta G^{0}_{f}(\mathrm{M^{2+}}) - 2y\Delta G^{0}_{f}(\mathrm{H^{+}}) + (x+y)\mu^{0}_{\mathrm{Ca}} - x\mu^{0}_{\mathrm{M}} - 2y\mu^{0}_{\mathrm{H_2}} \quad (3)$$

where μ^{0}_{Ca}, μ^{0}_{M} and $\mu^{0}_{\mathrm{H_2}}$ is chemical potentials of solid Ca, M, and H_2 gas. These values were considered to be the total energy calculated from first-pticiciples method. On the other hand, standard Gibbs formation energies of cations in solution were not calculated by first-principles calculations because calculations of hydrated ions in solution were too difficult. Instead of first-principles calculations, the values from thermodynamical database [17] were used. The last term was activity of solute ions. In this study, the activity coefficients were assumed to be unity. This is because HAp is poorly soluble and thus its saturated

solution could be regarded as dilute solution. To determine the solution concentration of Ca^{2+}, following conditions were assumed: saturated HAp solution, and charge neutrality. In these conditions Ca^{2+} concentration in HAp saturated solution were determined with pH, solubility product of HAp and acid dissociation constant of H_3PO_4, $H_2PO_4^-$, HPO_4^{2-} and PO_4^{3-}. Figure 2 shows Ca^{2+} concentration in HAp saturated solution. The concentration of M^{2+} was set to 1.0×10^{-4} mol/L of M^{2+}.

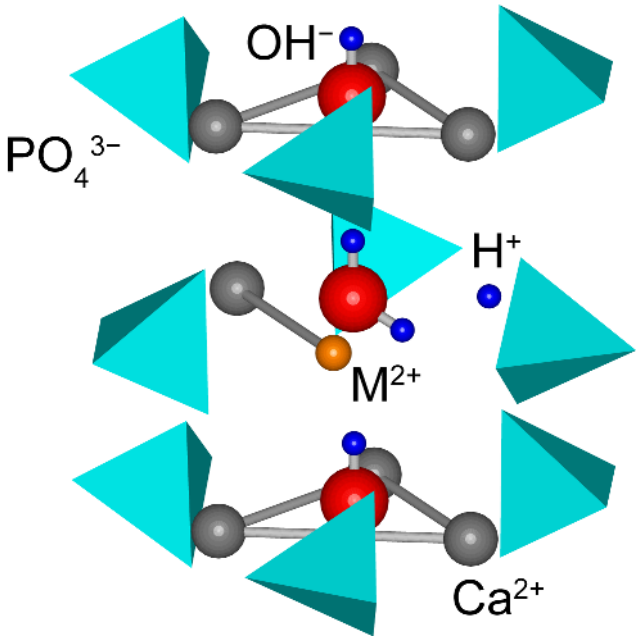

Figure 1 Initial positions of Ca^{2+}-deficient HAp model

Excess H^+ lies at the position of Ca^{2+} vacancies.

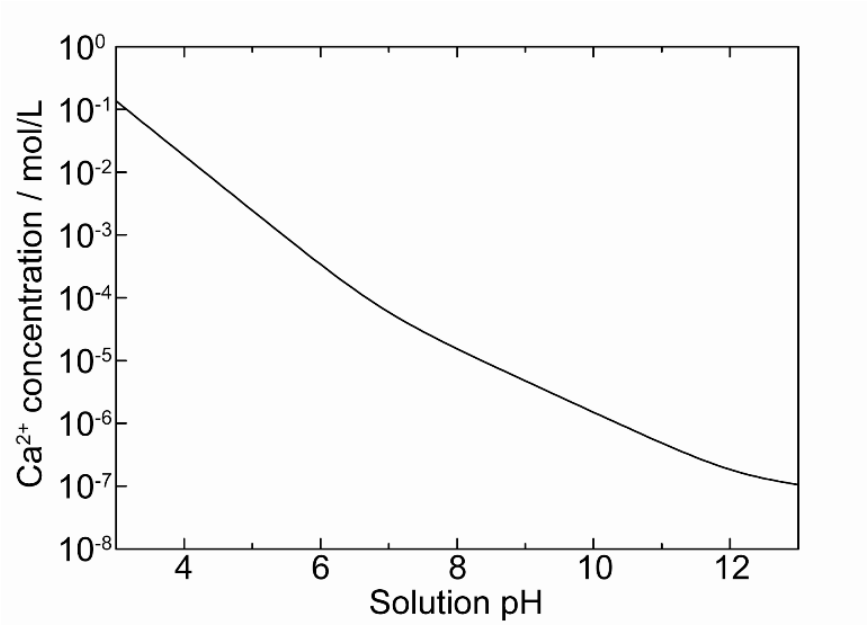

Figure 2 pH dependence of Ca^{2+} concentration in HAp saturated solution

3. Results and discussions

A. Local atomic and electronic structures around dopants

When defects were introduced, local atomic structures around defects were relaxed. In the present study, the local structures of solutes in Ca^{2+}-deficient HAp were classified into three structures, as shown in figure 3. For small ions, Zn^{2+} and Mg^{2+}, the H_2O moieties moved to them. For middle size ions, Ca^{2+} and Cd^{2+}, the H_2O moieties slightly moved. For larger ions, Ba^{2+}, Pb^{2+} and Sr^{2+}, the H_2O moieties moved to Ca^{2+} vacancies. In perfect HAp case, the OH^- groups scarcely relaxed for all of these cations. For example, the distance from original position of the H_2O moiety was 0.9 Å while that of OH^- group in perfect HAp model was 0.3 Å in the case of Ba^{2+}.For details analyses of local structure of dopants, figure 4 shows interatomic distances of oxygen ions and M^{2+} in perfect and Ca^{2+}-deficient HAp as a function of the ionic radii. In this study, Shannon's ionic radii of six-fold coordination [18] were used as ionic radii. Interatomic distance between M^{2+} and nearest neighbor oxygen ion, which was a part of PO_4^{3-} group, became short by formation of Ca^{2+}-vacancy. Other oxygen ions which were parts of PO_4^{3-} group also showed a similar tendency with some exception. On the other hand, interatomic distances between M^{2+} ions and oxygen ions have a different tendency, as shown in figure 5. They became long by formation of Ca^{2+} vacancy defect complex. The differences were depending on ionic radii, as shown in figure 6. It was interesting that changes of small ions were proportional to ionic radii while changes of large ions except Pb^{2+} has almost the same changes as Ca^{2+}. These structural relaxations might lead to the stabilization of solutes ion in Ca^{2+}-deficient HAp.

Figure 7 shows Local density of states (DOS) of defects in M^{2+}-doped Ca^{2+}-deficient HAp. Valence bands were mainly composed of O-2*p* band. For the case of Zn^{2+}, Cd^{2+} and Pb^{2+}, the contribution from these cations were included. On the other hand, Mg^{2+}, Ca^{2+}, Sr^{2+} and Ba^{2+} had little contribution to valence bands. In other words, cations which belong to same group in the periodic tables have similar electronic structure each other while local atomic structures had different feature, as discussed above. DOS of H_2O moiety were strongly affected by M^{2+} doping. On the other hand, DOS of HPO_4^{3-} were not affected by M^{2+}-doping. This indicated that the effects of M^{2+}-doping were localized. This is because HAp was ionic crystal, and thus,

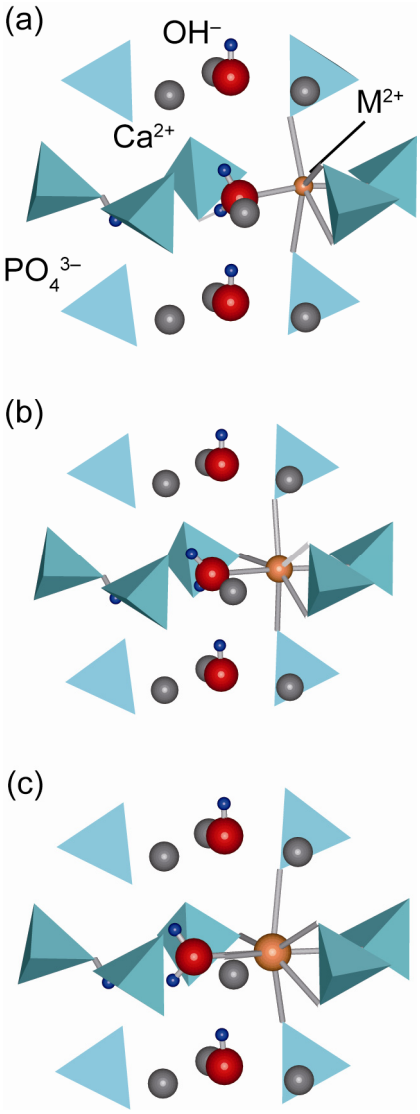

Figure 3 Schematic image of relaxed structure for (a) small ion, (b) middle size ion, and (c) large ion.

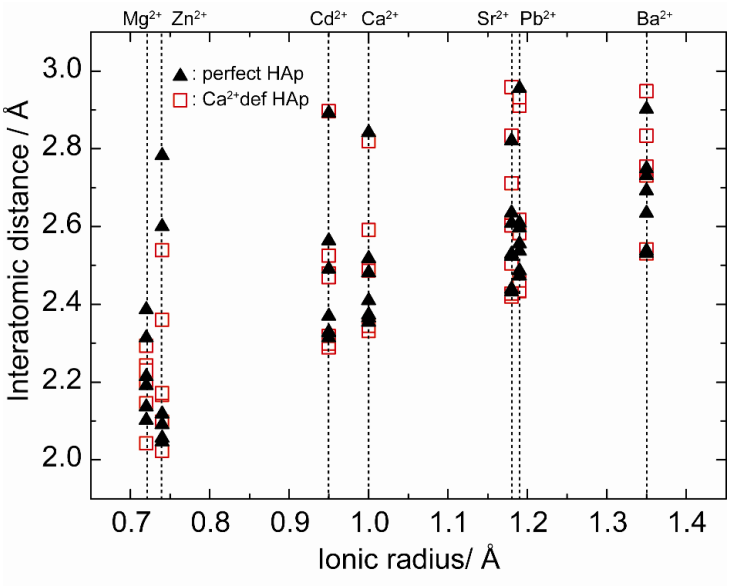

Figure 4 Interatomic distance between M^{2+} and oxygen ion in Ca^{2+}-deficient and perfect HAp model.

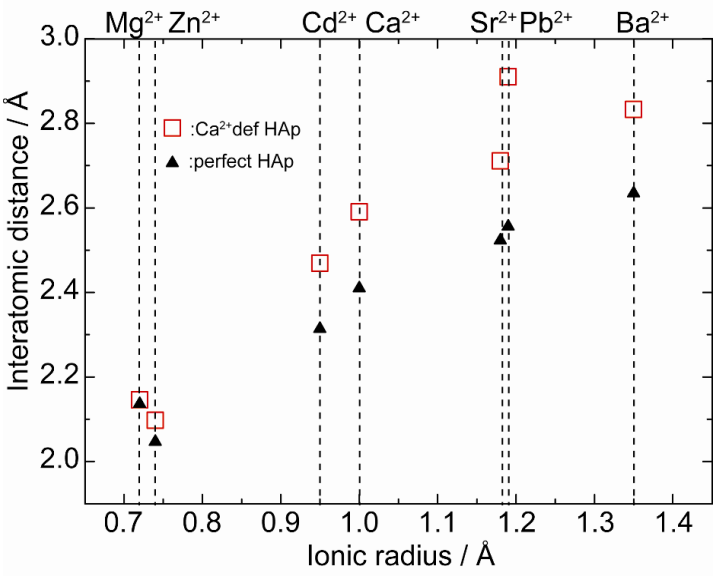

Figure 5 Interatomic distance between M^{2+} and oxygen ions which was part of H_2O moiety in Ca^{2+}-deficient HAp model. Interatomic distances between M^{2+} and OH^- group were also shown as reference.

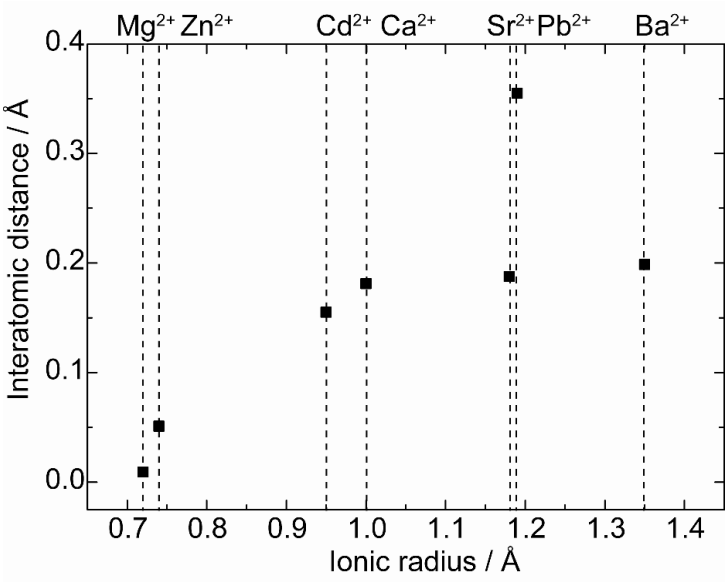

Figure 7 Differences of M^{2+}-H_2O in Ca^{2+}-deficient HAp and M^{2+}-OH in perfect HAp

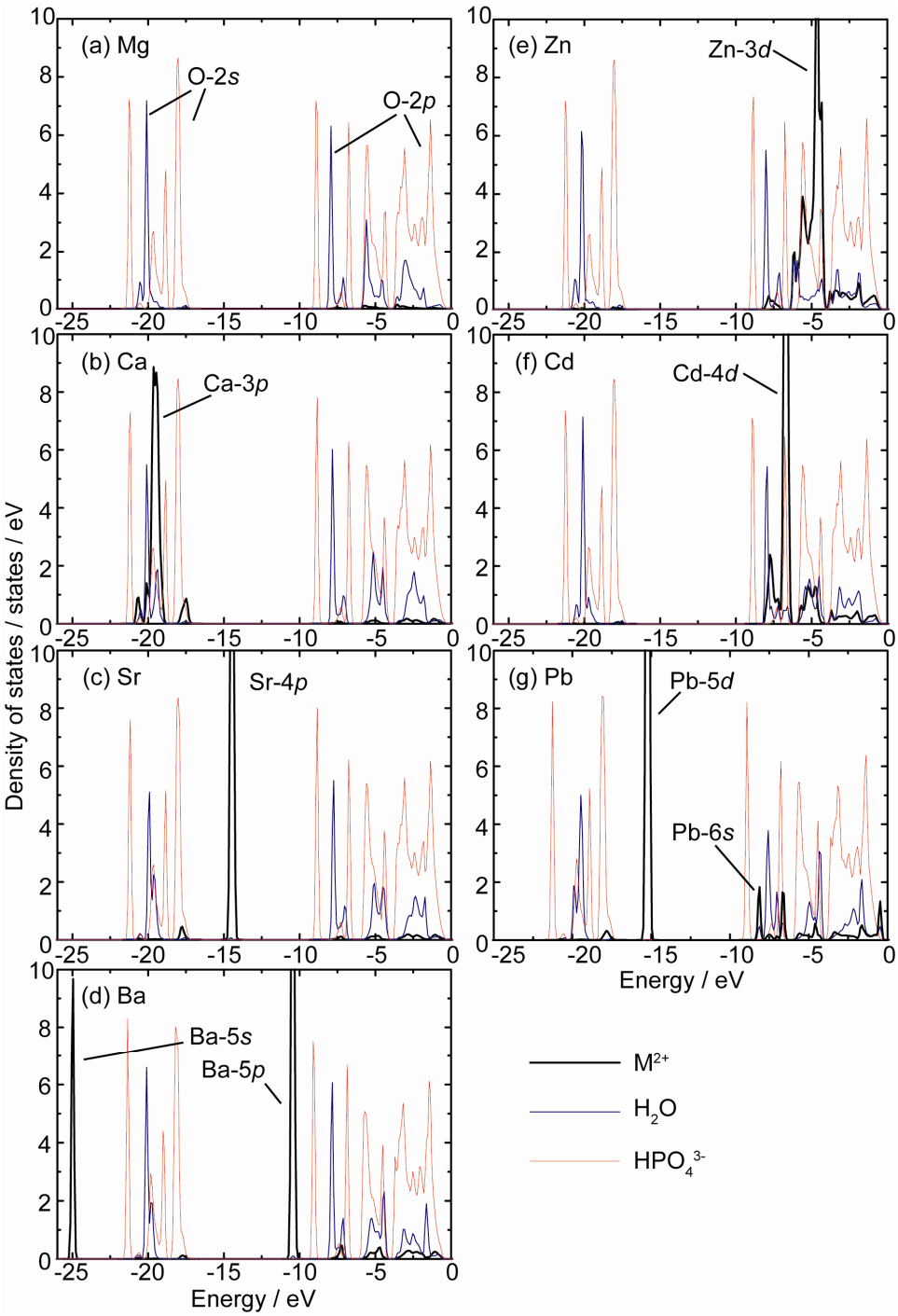

Figure 7 Local density of states of defects in M^{2+}-doped Ca^{2+}-deficient HAp

M^{2+} means (a) Mg^{2+}, (b) Ca^{2+}, (c) Sr^{2+}, (d) Ba^{2+}, (e) Zn^{2+}, (f) Cd^{2+} and (g) Pb^{2+}, respectively. Zero was set to the valence band maxima.

B. Defect formation energy

Figure 8 shows the calculated defect formation energies of perfect and Ca^{2+}-deficient HAp models. It was found that pH dependence of ionic substitution energies showed different features between perfect and Ca^{2+}-deficient HAp models. In perfect HAp models, pH did not contribute directly. However, the concentration of Ca^{2+} was depended on pH, and thus the ionic substitution energies were reduced as pH increase. On the other hand, the substitution energies of Ca^{2+}-deficient HAp model include concentration of H^{+} as activity terms. Therefore, pH directly affected to the substitution energies.

The defect formation energies were reduced except Cd^{2+} and Pb^{2+}. These two cations have low substitution energies in perfect HAp model. The formation energies of Ca^{2+} vacancies defect complex were positive number, and thus, incorporation of into HAp with Ca^{2+} vacancy defect complex demand extra energies for Cd^{2+} and Pb^{2+}. It was noted that present calculations assumed the model which was found in the previous chapter. Therefore, there might be configurations which reduce defect formation energies of Cd^{2+} and Pb^{2+}.

Figure 9 shows difference of defect formation energies between Ca^{2+}-deficient and perfect HAp model as a function of difference of ionic radius between M^{2+} and Ca^{2+}. Except Cd^{2+} and Pb^{2+}, defect formation energies were reduced as whether ionic radius was larger or not than that of Ca^{2+}. This implied that Ca^{2+}-vacancy defect complex permit to extra structural relaxations, and thus, the structural relaxation was important factor for decrement of defect formation energies.

As discussed above, local atomic structures were classified by ionic radii

of M^{2+} while the positions in the periodic tables were important for electronic structures. Even if the electronic structure resembled each other, defect formation energies were different. On the other hand, cations which have close ionic radii to Ca^{2+} have low defect formation energies. This indicated that the local atomic structures were important factor to doping into HAp.

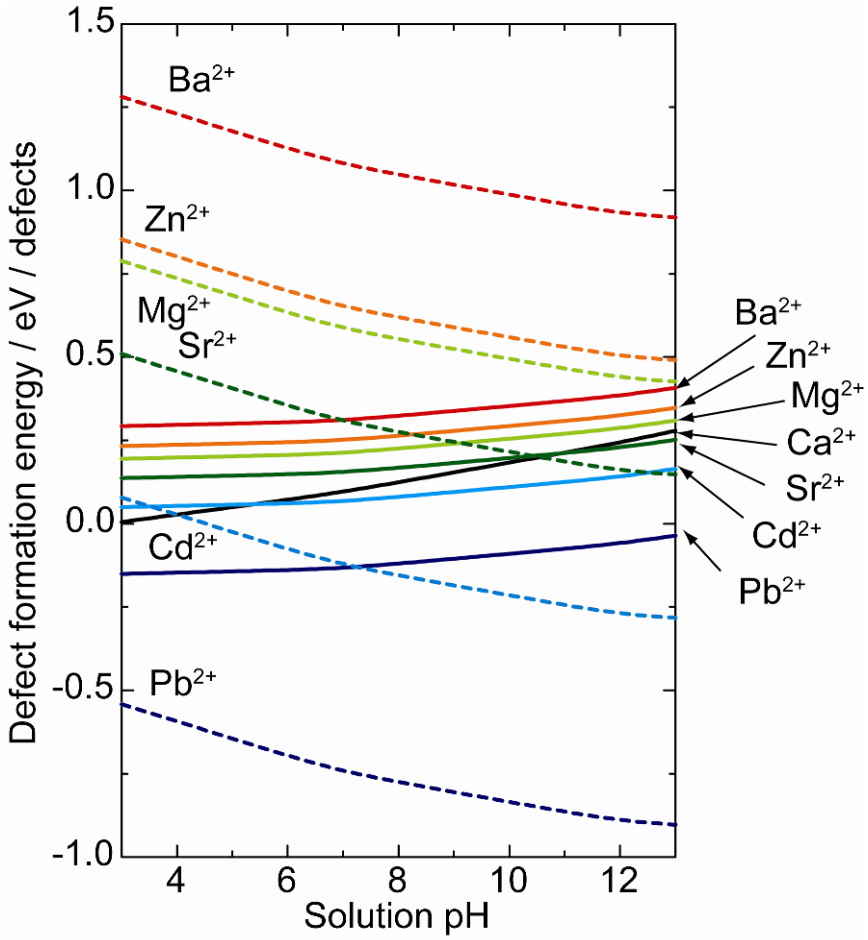

Figure 8 Defect formation energies of M^{2+} into perfect and Ca^{2+}-deficient HAp

Dashed lines mean perfect HAp model and solid lines mean Ca^{2+}-deficient HAp model

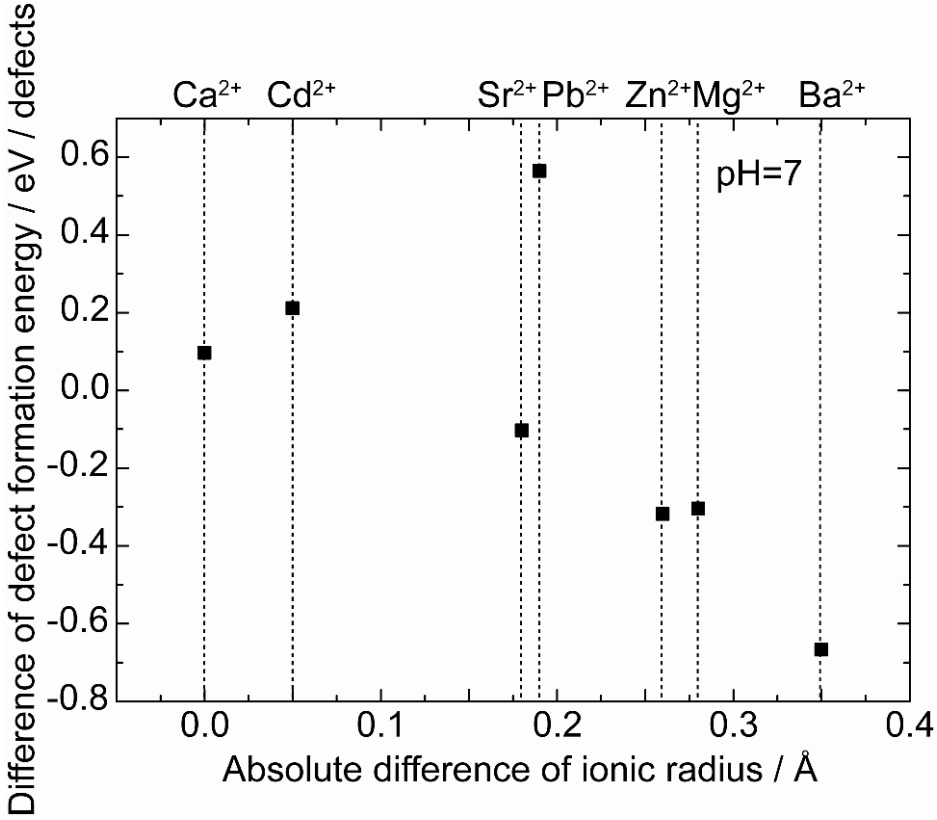

Figure 9 Relationship of ionic radius differences of Ca^{2+} and M^{2+} and defect formation energies

4. Summary

Effects of Ca^{2+}-vacancies to incorporation into HAp of divalent cations Mg^{2+}, $Sr2^{+}$, Ba^{2+}, Zn^{2+}, Cd^{2+} and Pb^{2+}, were investigated by first-principles calculations. Formation of Ca^{2+} defect complex enables these solutes and surrounding atoms to be further optimized. Interatomic distances between M^{2+} and oxygen ions which were parts of PO_4^{3-} became short while that of H_2O moiety were extended. On the other hand, electronic structures of defects were classified by the group in the periodic table while local atomic structures resembled each other.

Defect formation energies of solute ions were reduced by incorporation with Ca^{2+}-vacancy defect complex except Cd^{2+} and Pb^{2+}. These two cations have low substitution energies into perfect HAp model, and thus, it was useless for them to incorporation with Ca^{2+}-vacancy defect complex. For other cations, the gain of free energy was a function of difference between ionic radii of Ca^{2+} and M^{2+}. This implied that Ca^{2+}-vacancy defect complex permit to extra structural relaxations, and thus, structural relaxation was important factor for decrement of defect formation energies.

References

[1] J. C. Elliott, Structure and Chemistry of the Apatites and Other Calcium Orthophosphates, Amsterdam, Elsevier, (1994).

[2] B. Bourgeois, O. Laboux, L. Obadia, O. Gauthier, E. Betti, E. Aguado, G. Daculsi and J. M. Bouler, J. Biomed. Mater. Res. 64A, 402-408 (2003).

[3] K. Matsunaga, J. Am. Ceram. Soc. 93, 1-14 (2010).

[4] D. Zahn and O. Hochrein, J. Sol. State Chem. 181, 1712 (2008).

[5] K. Matsunaga and A. Kuwabara, Phys. Rev. B 75, 014102 (2007).

[6] K. Matsunaga, H. Inamori and H. Murata, Phys. Rev. B 78, 094101 (2008)

[7] J. Terra, E. R. Dourado, J. G. Eon, D. E. Ellis, G. Gonzalezd and A. M. Rossia, Phys. Chem. Chem. Phys. 11, 568-577 (2009)

[8] K. Matsunaga and H. Murata, J. Phys. Chem. B 113, 3584-3589 (2009).

[9] K. Kawabata and T. Yamamoto, J. Ceram. Soc. Japan 118, 548-549 (2010).

[10] P. E. Blochl, Phys. Rev. B 50 17953 (1994).

[11] G. Kresse and J. Furthmuller, Phys. Rev. B 54, 11169 (1996).

[12] G. Kresse and J. Furthmuller, Comput. Mater. Sci. 6 15 (1996).

[13] G. Kresse G and D. Joubert, Phys. Rev. B 59, 1758 (1999).

[14] H. J. Monkhorst and J. D. Pack, Phys. Rev. B 13, 5188 (1976).

[15] J. P. Perdew, K. Burke and M. Ernzerhof, Phys. Rev. Lett. 77, 3865 (1996).

[16] K. Momma and F. Izumi, J. Appl. Cryst. 41, 653-658 (2008).

[17] D. D. Wagman, W. H. Evans, V. B. Parker, R. H. Schumm, I. Halow, S. M. Bailey, K. L. Churney, and R. L. Nuttall, J. Phys. Chem. Ref. Data 11, 1 (1982).

[18] R. A. Shannon, Acta Crystallogr., Sect. A: Cryst. Phys., Diffr., Theor. Gen. Crystallogr. 32, 751 (1976).

Chapter 4

Lattice dynamics and thermal properties of Sr^{2+}-doped hydroxyapatite

1. Introduction

Hydroxyapatite ($Ca_5(PO_4)_3OH$, HAp) is a main inorganic component of human bones and teeth. HAp in human body has various kinds of defects and impurities. They affect biological properties of HAp. Attempts to improve biological properties of HAp by doping have been reported [1]. Therefore, it is important to investigate electronic and atomic structures of dopants in HAp.

Sr^{2+} is one of important dopants for HAp. It was also found in human body. The amounts of Sr^{2+} in human bones, dentine and enamel were 0.05 wt%, 0.04 wt% and 0.03 wt%, respectively [2]. Sr^{2+} affects various kinds of properties of HAp. Pan et al. measured solubility of Sr^{2+}-doped HAp systematically [3]. They reported solubility of HAp increased as Sr^{2+} content increase. It was also considered that Sr^{2+} has an important role for biological properties of HAp. Aoki et al. studied Sr^{2+} content of femur bones of rats which were exercised for four weeks [4]. Femur bones of exercised group contained more Sr^{2+} than control group. They also reported that the bones became strong at the same time. Sr^{2+} affected activities of osteoclasts and osteoblasts, which were the cell that were related to bone-remodling [5].

Sr^{2+}-doped HAp was synthesized with various methods, the

solution-precipitation method [6], the hydrothermal method [7, 8] and the solid-state reaction method [9]. Sr^{2+} could make whole range solution into HAp synthesized by these methods [6-7, 9]. Local environment of Sr^{2+} in HAp also attracts interest of many researchers. Zhu et al. investigated site preference of Sr^{2+} in HAp synthesized by hydrothermal method at 473 K [7]. They reported that Sr^{2+} was substituted for both Ca-1 and Ca-2 sites but Ca-2 site was slightly preferential site. O'Donnell et al. also reported Raman and Rietveld analysis on Sr^{2+}-doped HAp synthesized by wet chemical reaction method [6]. They also reported that Ca-2 site was slightly preferential site. Terra et al. also investigated Sr^{2+}-doped HAp [8]. It was reported that Ca-1 site were preferred to Ca-2 site when Sr^{2+} contents were below 1 at%. For higher concentration of Sr^{2+}, Ca-2 site was progressively preferred. Although preparation temperature of Sr^{2+}-doped HAp varied wide ranges, from room temperature to over 1273 K, the temperature effect to local environment of Sr^{2+} in HAp was not reported.

From theoretical point of view, first-principles calculations of Sr^{2+}-doped HAp were carried out by several groups [9-13]. Our previous calculations showed that Sr^{2+} preferred Ca-1 site when the chemical equilibrium between HAp and aqueous solution of diluted Sr^{2+} concentration was assumed [10-12]. Terra et al. considered configurations of Sr^{2+}, i.e., Sr^{2+} substituted for Ca-1 site, Ca-2 site and both of these sites. They concluded that Ca-1 site had the lowest substitutional energy of them. These calculations could not well explain Sr^{2+} substituted for Ca-2 site. There might be some reasons. For example, the effects of temperature were not considered.

First-principles method usually treated electronic states at ground state,

and thus, temperature effects were not included. Recent progresses of both algorithms and hardware enable us to calculate lattice vibration or phonon with first-principles manner. This method, called first-principles lattice dynamics calculation, was powerful tool to investigate lattice vibration and thermal properties of ceramics materials under finite temperature. For example, thermal properties and phase transitions of ZrO_2 [14] and Si_3N_4 [15] were investigated. This method also applied to dopants in ceramics materials such as Ag^+ in potassium halides [16] and Fe in CoO [17].

In this chapter, temperature effects to Sr^{2+}-doped HAp were investigated. Experimentally, Sr^{2+}-doped HAp samples were synthesized different temperature and local environments of its Sr^{2+} were analyzed with X-ray absorption nears edge structures (XANES). These experiments suggested that the substitution site of Sr^{2+} were changed depending on synthesis temperature. Theoretically, first-principles lattice dynamics calculations of Sr^{2+}-doped HAp were carried out. Contribution of phonon stabilized Sr^{2+} substituted for Ca-2 site while Sr^{2+} substituted for Ca-1 site was stable at ground state. It was found that thermal effects could change Sr^{2+} substitution site.

2. Calculation methods

Electronic and atomistic structures were calculated by projector augmented wave (PAW) method [18] implemented by VASP code [19-21]. Cut-off energy of plane waves was set to 500 eV. The *k*-points sampling were performed by Γ-centered Monkhorst-Pack 2×2×1 mesh [22] for 1×1×2 supercell of hexagonal HAp. Details of calculated models were discussed below. The initial electronic configurations were for Sr, Ca, H, P and O, $4s^2 4p^6 5s^2$, $3s^2 3p^6 4s^2$, $1s^1$ and $3s^2 3p^3$ respectively. Exchange-correlational functional were evaluated by local density approximation (LDA) and generalized gradient approximation proposed by Perdew, Burke and Ernzerhof (GGA-PBE) [23]. Lattice constants and internal atomic positions were fully optimized until residual forces became less than 1.0×10^{-3} eV / Å.

For Sr-K XANES calculations, the optimized atomic structures for substitutional Sr^{2+} in HAp by the above PAW calculations with GGA-PBE were used, and the full-potential augmented plane wave + local orbitals method (WIEN2k code [24]) in this study. A core-hole was directly treated for final state calculations [25]. The dipole transition was considered as the selection rule. The transition energies were evaluated with the difference of total energies in final and initial (ground) states. The difference of transition energies between experiment and calculations were corrected with the value of reference material, $SrCO_3$. The R_{MT} of each element was set to 1.50, 1.50, 1.45, 1.19 and 0.64 for Sr, Ca, P, O and H, respectively. The $R_{MT}K_{MAX}$, the cut-off parameter of the plane wave, was set to 3.5 bohr $Ry^{1/2}$. The exchange-correlation functional was evaluated with GGA-PBE and *k*-point mesh was the same conditions as used in the structural optimizations

described above.

Calculated models were based on 1×1×2 supercell of hexagonal HAp primitive cell. In Sr^{2+}-doped HAp models, one Sr was substituted for Ca in supercell. As discussed at chapter 2, the space group of hexagonal HAp is $P6_3/m$ with half occupancies of OH^- direction. The ordered model were also stable than faced model in LDA calculation. Therefore, the ordered column model was employed in this study. Table 1 showed relaxed structural parameters of pure HAp. Under these conditions, lattice parameters were within the usual LDA and GGA errors.

Lattice dynamics calculations were performed by Parlinski-Li-Kawazoe method [27] implemented by phonopy code [28]. In this method, phonon frequencies were calculated via force constants. Under harmonic approximation, force constants were calculated from forces acting on atoms when small displacements were added on atoms.

In this study, Helmholtz free energy of the system $F_{system}(T)$ was evaluated by following formula:

$$F_{system}(T) = E_0 + F_{phonon}(T) - TS_{config} \quad (1)$$

where T is temperature, E_0 is the total energy of electronic system, $F_{\mathrm{phonon}}(T)$ is free energy of phonon and S_{config} is configuration entropy. In the present study, Ca-1a and Ca-1b sites identified as Ca-1 site for calculations of configuration entropy. This was because experimental hexagonal HAp has only one Ca-1 site, and thus, configuration entropy term was underestimated if Ca-1a and Ca-1b sites were distinguished.

In canonical ensemble, Helmholtz free energies $F(T)$ were given by

following formula:

$$F(T) = -k_B T \ln Z \tag{2}$$

where Z is distribution function and k_B is Boltzmann's constants. The distribution function of phonon was given by following formula:

$$Z = \sum_{\{n_j(\mathbf{k})\}} \exp\left(-\beta E\left\{n_j(\mathbf{k})\right\}\right) = \prod_{\mathbf{k},j} \frac{\exp\left[-\frac{1}{2}\beta\hbar\omega_j(\mathbf{k})\right]}{1-\exp\left[-\beta\hbar\omega_j(\mathbf{k})\right]} \tag{3}$$

where $\omega_j(\mathbf{k})$ is the j th eigenfrequency of phonon at **k** and $\beta = \frac{1}{k_B T}$. Therefore, Helmholtz free energy of phonon $F_{phonon}(T)$ was

$$F_{phonon}(T) = rk_B T \int_0^\infty \ln\left[2\sinh\left(-\frac{\hbar\omega}{2k_B T}\right)\right] g(\omega) d\omega \tag{4}$$

where $g(\omega)$ is phonon density of states (DOS) and $g(\omega)$ is normalized by degrees of freedom *r*, i.e.,

$$\int_0^\infty g(\omega) d\omega = \frac{1}{r}. \tag{5}$$

Using this formula, the temperature and frequencies dependence of Helmholtz free energy of phonons were shown in figure 2. Free energy of phonon at 0 K, zero point energy, increased as frequencies increase. On the other hand, the temperature dependence of free energy was large at low frequency region, while it is small at high frequency region. Therefore, phonons which have low frequencies are important for stabilities of the system at high temperature.

It is noted that these formalism were assumed canonical ensemble, and thus, variable parameters were *V* and *T*. Contribution of volume change *p*d*V* which

was occurred by impurities doping should be considered. Therefore, both of cell relaxation models and cell fixed models were calculated in the present study.

Table 1 Structure parameters of pure HAp

		Present calc.		Expt.[a]
		GGA-PBE	LDA	
Space Group		$P6_3$		$P6_3/m$
a (Å)		9.566	9.260	9.432
c (Å)		6.904	6.767	6.881
Ca-1[b]	Ca-1a	1/3, 2/3, 0.003	1/3, 2/3, 0.002	1/3, 2/3, 0.0014(4)
	Ca-1b	1/3, 2/3, 0.500	1/3, 2/3, 0.499	1/3, 2/3, 0.4986(4)
Ca-2		0.251, 0.000, 0.250	0.246, 0.000, 0.251	0.2466(2), 0.9931(2), 1/4
P		0.400, 0.369, 0.249	0.399 0.367, 0.250	0.3982(2), 0.3682(2), 1/4
O1		0.333, 0.487, 0.248	0.327, 0.485, 0.248	0.3283(2), 0.4846(2), 1/4
O2		0.588, 0.464, 0.254	0.592, 0.467, 0.256	0.5876(2), 0.4652(2), 1/4
O3		0.345, 0.260, 0.066	0.349, 0.256, 0.064	0.3433(1), 0.2579(1), 0.0705(2)
O4		0, 0, 0.216	0, 0, 0.211	0, 0, 0.2008(7)
H		0, 0, 0.074	0, 0, 0.065	0, 0, 0.0617(15)

[a] reference 26

[b] Because of lack of mirror plane in ordered model, Ca-1 site of hexagonal HAp was divided into two sites, Ca-1a and Ca-1b

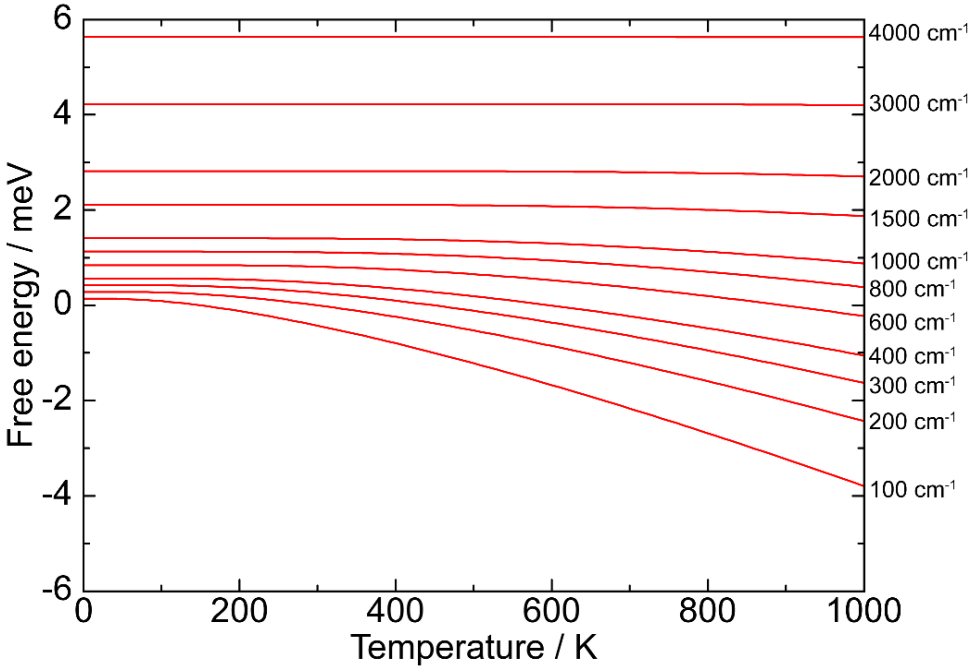

Figure 1 Helmholtz free energy depending on phonon frequencies.

3. Experimental procedures

To investigate the effect of temperature, Sr^{2+}-doped HAp (HAp:Sr^{2+}) were synthesized at various temperature. In this study, the solid-state reaction method and the aqueous precipitation method were adapted. For solid-state reaction method, $SrCO_3$ (Kojundo chemical laboratory CO., LTD, 99.9%), $CaCO_3$ (Kojundo chemical laboratory CO., LTD, 99.9%) and $CaHPO_4 \cdot 2H_2O$ (Nakalai tesque, Guaranteed Reagent) were used as starting materials. The ratio of Sr and Ca was set to 1:99. Starting materials were ground and mixed with alumina mortar. Mixed powders were calcined at 1273 K for 6 hours in air. Calcined powders were ground and mixed again. Then, they were pressed into pellet by mono-axial press. Finally, they were calcined at 1523 K for 3 hours in air.

For the aqueous-precipitation method, $Ca(NO_3) \cdot 4H_2O$ (Wako pure chemical industries, LTD, 99.9%), $Sr(NO_3)_2$ (Wako pure chemical industries, LTD, 99.9%) and $(NH_4)_2HPO_4$ (Wako pure chemical industries, LTD, special grade) were used as starting materials. At first, 0.1 mol/L aqueous solutions of the stating materials were made. Then, 60 ml of the $(NH_4)_2HPO_4$ solution was dropped into 100 ml of the $Ca(NO_3)_2$ and $Sr(NO_3)_2$ solutions. In this case, the ratio of Ca to Sr was set to 99:1. The solution was mixed with the magnetic stirrer and matured for 24 hours. During mixing and maturing, solution pH was kept to 10 at room temperature. After maturing, the samples were filtrated, washed by ultrapure water and dried at 323 K for 12 hours.

The obtained samples were analyzed with powder X-ray diffraction (XRD), Fourier transform infrared spectroscopy (FTIR) and XANES. The XRD data were collected with the Bragg-Brentano-type diffractometer (Smart Lab.,

Rigaku Corporation) using Cu-Kα radiation (40 kV and 30 mA). The divergence slit (DS), the scattering slit (SS) and the receiving slit (RS) were set to 1/2°, 1/2°, 0.30 mm, respectively. FTIR measurements were carried out with JASCO FT/IR-6200. At first, the samples were dried at 383 K and diluted with KBr and then pressed into pellets. Local environment of Sr^{2+} in HAp were investigated by XANES. Experimental Sr-K XANES spectra were measured by the transmission mode with using the ion-chambers at BL01B1 in SPring-8, Harima, Japan. In the XANES measurements, X-ray beam was monochromatized with Si-(311) double crystals.

4. Results and discussion

A. Experiment

Figure 2 shows XRD patterns obtained from synthesized HAp:Sr^{2+}. All of the peaks can be assigned to those from pure HAp (JCPDS-01-072-1243 [29]), which indicates no secondary phase in the present samples. Stoichiometric HAp often shows the ordering of OH^- and then phase transition to monoclinic structure is occurred. This monoclinic HAp was characterized with the reflection such as 112 ($2\theta = 29.72$) and 212 ($2\theta = 36.28$). However, these peaks were not measured in the present study. Therefore, our Sr^{2+}-doped HAp samples synthesized by the solid-state reaction method was hexagonal HAp. On the other hand, the profile of sample synthesized with aqueous-precipitation method was somewhat broad, but it was often found for samples obtained by the similar low temperature process [1].

FT-IR spectra of Sr^{2+}-doped HAp samples were shown in figure 3. They showed typical features of HAp phase but they had slightly broad and shifted spectra. In the sample prepared by the solution-precipitation method, there were two differences from reference sample, the broad absorption around 3500 cm^{-1} and the peak around 875 cm^{-1}. The former was the absorption of H_2O in HAp crystals, which was often seen in HAp synthesized at low temperature. The latter was assigned to the band of CO_3^{2-}, which was incorporated into HAp during the synthesis.

Local environments of Sr^{2+} in HAp were examined with Sr-K XANES measurements. Figure 4 shows experimental Sr-K XANES spectra. HAp:Sr^{2+} synthesized by solid-state reaction method had different feature from samples synthesized by the aqueous-precipitation method. HAp:Sr^{2+} synthesized by the

solid-state reaction method have a peak at 16115 eV, while HAp:Sr^{2+} synthesized by the aqueous-precipitation method did not have..

To investigate the origin of peaks at 16115 eV, Sr-K XANES of Sr^{2+}-doped HAp was calculated by first-principles supercell method with a core-hole effect. Calculated Sr-K XANES were shown in figure 4. Sr^{2+} substituted for Ca-2 site had a peak at 16115 eV while Sr^{2+} substituted for Ca-1 site did not have. Therefore, this peak indicated the amount of Sr^{2+} substituted for Ca-2 site. HAp:Sr^{2+} synthesized by solid state reaction method contained much more Sr^{2+} substituted for Ca-2 site than HAp:Sr^{2+} synthesized by precipitation method.

Terra et al. reported that Sr^{2+} was substituted for Ca-1 site in 1at% Sr^{2+}-doped HAp synthesized precipitation method [8]. Sr-K XANES analysis gave the same results for HAp:Sr^{2+} synthesized by precipitation method. On the other hand, HAp:Sr^{2+} synthesized solid-state reaction method contains large quantity of Sr^{2+} substituted for Ca-2 site, while the composition of Sr^{2+} was the same as HAp:Sr^{2+} synthesized by aqueous-precipitation method. Therefore, it is possible for temperature to work as a factor to determine substitution site of Sr^{2+}.

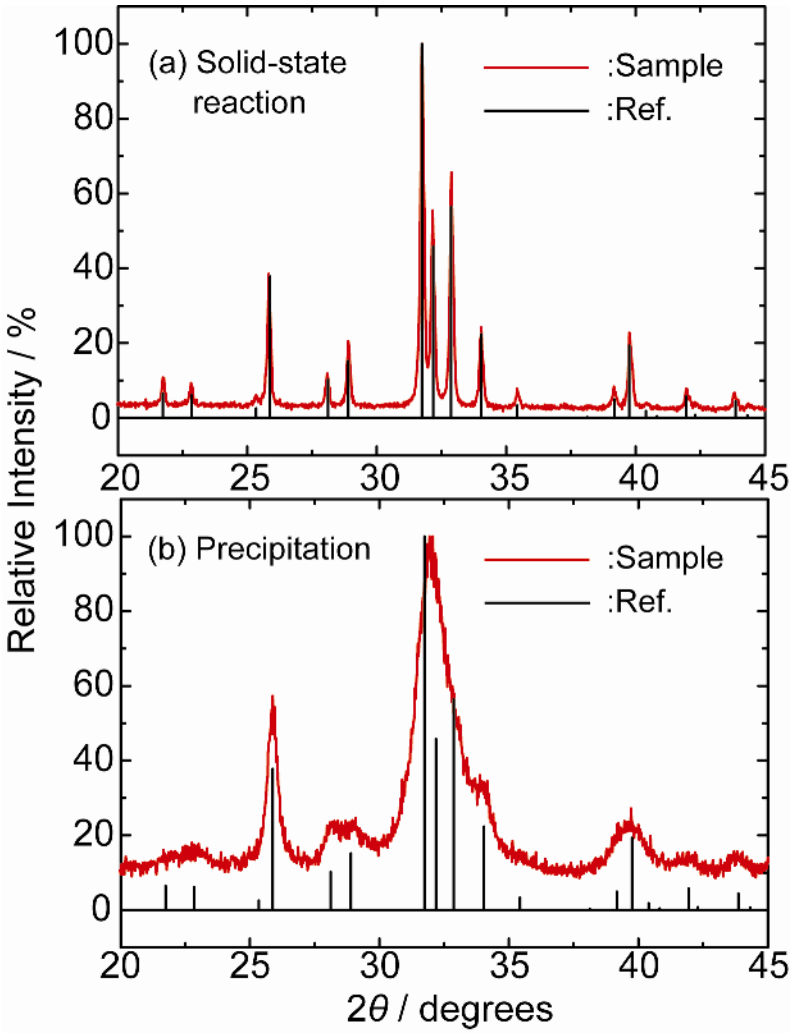

Figure 2 XRD pattern of Sr^{2+}-doped HAp

(a) HAp:Sr^{2+} synthesized by the solid-state reaction method and (b) HAp:Sr^{2+} synthesized by the aqueous precipitation method. Red lines were samples and black lines were reference pattern of pure HAp (JCPDS 01-072-1243 [29])

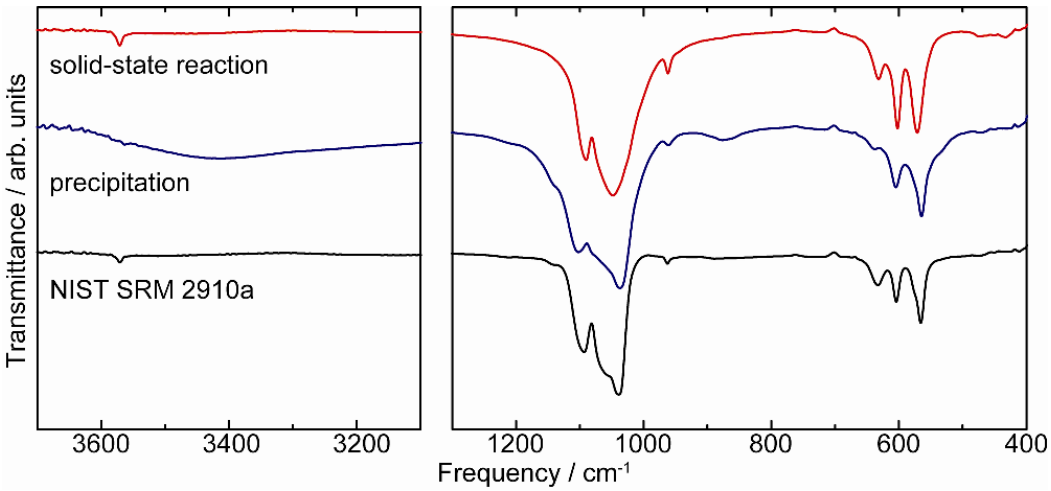

Figure 3 FT-IR spectra of Sr^{2+}-doped HAp

Red line was the spectrum of Sr^{2+}-doped HAp synthesized by the solid-state reaction method, blue line was that of Sr^{2+}-doped HAp synthesized by the solution-precipitation method and black line was the spectrum of NIST SRM 2910a (hydroxyapatite)as reference.

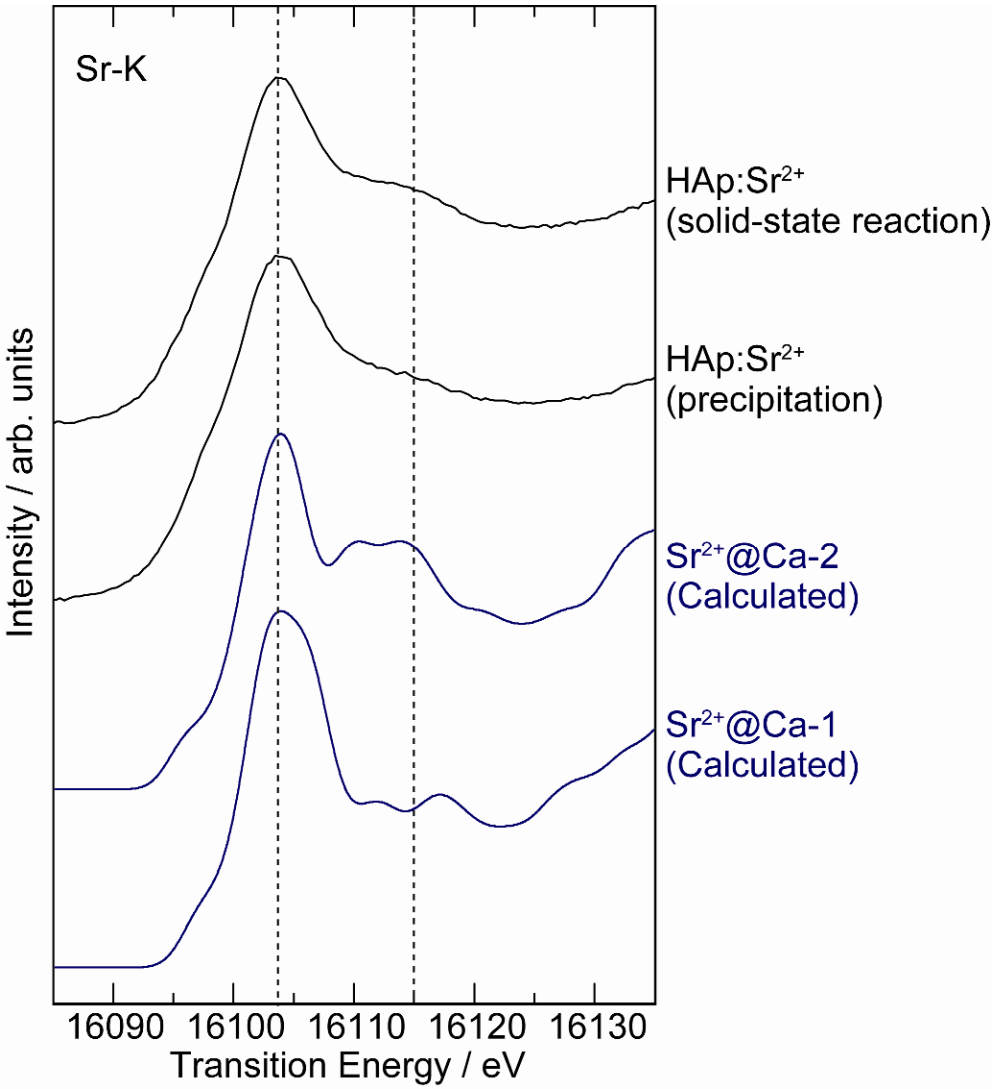

Figure 4 Experimental and calculated Sr-K XANES spectra

Black lines were experimental Sr-K XANES and blue lines were calculated ones

B. Calculation

Structures and Energies at ground state

In order to investigate details of temperature effect, first-principles lattice dynamics calculations were carried out. At first, optimized structure at ground states were discussed on. Structural parameters and relative substitutional energies of Sr^{2+}-doped HAp were shown in Table 2. Sr^{2+} doping increased lattice parameters and cell volume when cell relaxations were carried out. The model that Sr^{2+} substituted for Ca-2 site has longer *a*-axis and bigger volume than Sr^{2+} substituted for Ca-1 site, while *c*-axis of the model that Sr^{2+} substituted for Ca-2 site was shorter than that of Ca-1 site.

Figure 5 and 6 summarized Sr-O bond length of calculated by GGA-PBE and LDA, respectively. Among these bonds, Ca-2 site had minimum bond length. Therefore, Ca-2 site was smaller than Ca-1 site. It was noted that Ca-O bond lengths were significantly different between Ca-1a and Ca-1b sites. Therefore, Ca-1b site was the biggest site. These tendencies were kept when Sr^{2+} substituted for Ca-site. It was interesting that interatomic distance between Sr^{2+} and oxygen was almost same whether cell was relaxed or not.

Among these sites, Sr^{2+} substituted for Ca-1b site was most stable. Sr^{2+} has larger ionic radius than Ca^{2+}, and thus, it was natural that Sr^{2+} substituted for biggest site was most stable. Moreover, cell relaxation decreases difference of substitution energies between Ca-1 and Ca-2 sites. Thus, the expansion of cell stabilized Ca-2 site. This might be one of the reasons for site changes of Sr^{2+} substitution site depending on Sr^{2+} composition.

Since Sr^{2+}-doping changed cell volume of HAp, contribution of these

volume changes to enthalpy should be considered. Without cell relaxation, Sr^{2+}-doping caused strong stress in cell fixed model. External pressures were around 5 kbar, which was evaluated from these stresses. On the other hand, volume difference between Sr^{2+} substituted for Ca-1 and Ca-2 was only 1 $Å^3$ and thus, the contribution of these volume change to enthalpy were less than 10 meV and thus, the contribution of volume changes were neglected in this study..

Table 2 Lattice parameters of Sr^{2+}-doped HAp

E_{xc}	Cell	Site	*a* (Å)	*c* (Å)	*V* (Å^3)	Relative Energy (eV)
GGA-PBE	fixed	Ca-1a	9.566	6.904	547.0	0.083
		Ca-1b				0.027
		Ca-2				0.106
	relaxed	Ca-1a	9.572	6.935	550.3	0.055
		Ca-1b	9.566	6.939	549.9	0.000
		Ca-2	9.596	6.919	551.3	0.073
LDA	fixed	Ca-1a	9.260	6.767	502.5	0.093
		Ca-1b				0.023
		Ca-2				0.157
	relaxed	Ca-1a	9.273	6.791	505.7	0.068
		Ca-1b	9.269	6.793	505.4	0.000
		Ca-2	9.281	6.784	506.0	0.129

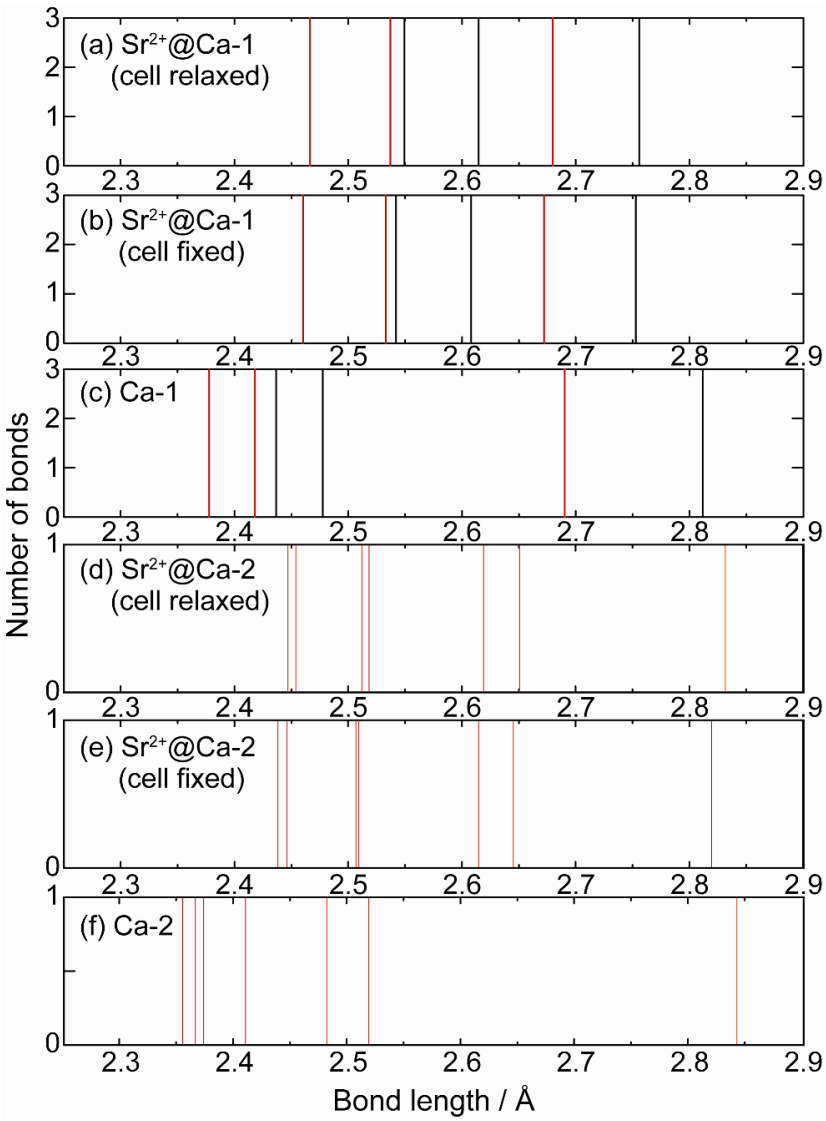

Figure 5 Sr-O and Ca-O bond length in Sr^{2+}-doped HAp and pure HAp calculated with GGA-PBE

Sr^{2+} substituted for Ca-1 site in (a) cell relaxed model and (b) cell fixed model, (c) Ca-1 site of pure HAp, Sr^{2+} substituted for Ca-2 site in (d) cell relaxed model and (e) cell fixed model and (f) Ca-2 site in pure HAp. For Ca-1 sites, red lines were Ca-1a site and black lines were Ca-1b site.

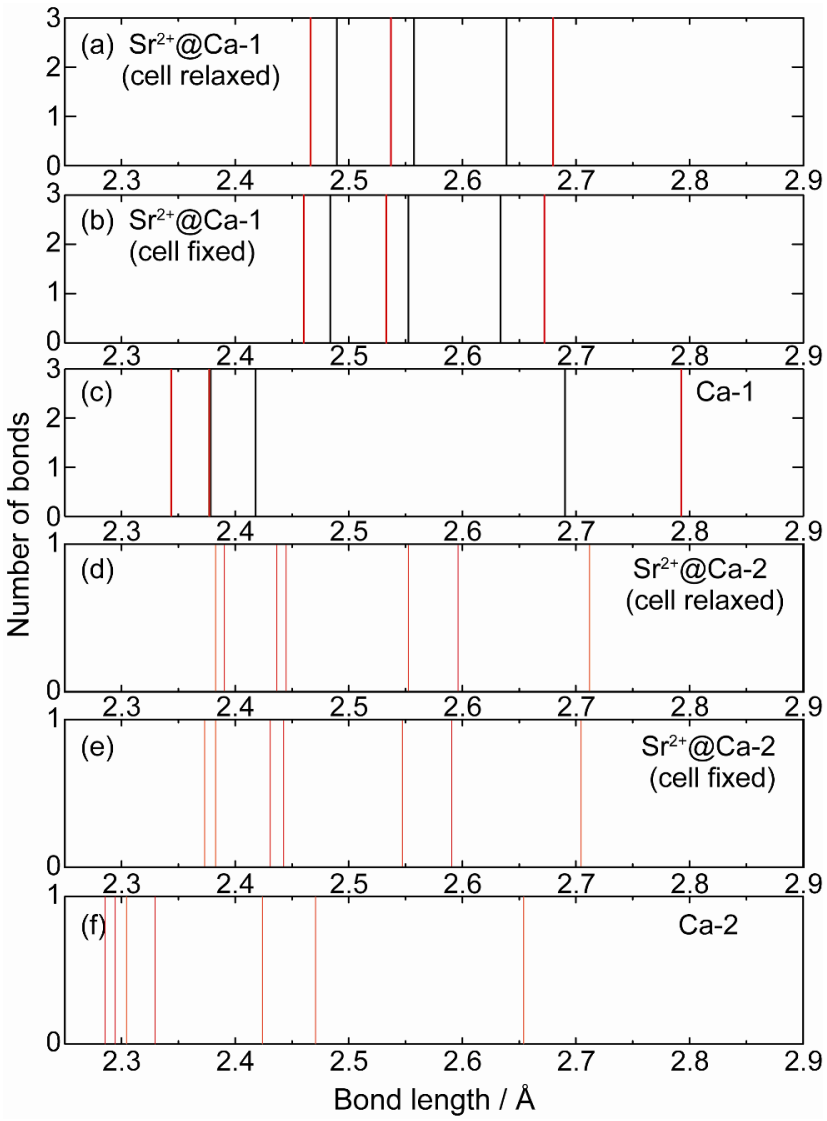

Figure 6 Sr-O and Ca-O bond length in Sr^{2+}-doped HAp and pure HAp calculated with LDA

Sr^{2+} substituted for Ca-1 site in (a) cell relaxed model and (b) cell fixed model, (c) Ca-1 site of pure HAp, Sr^{2+} substituted for Ca-2 site in (d) cell relaxed model and (e) cell fixed model and (f) Ca-2 site in pure HAp. For Ca-1 sites, red lines were Ca-1a site and black lines were Ca-1b site.

Lattice dynamics and thermal properties of pure HAp

Then, lattice dynamics and thermal properties of pure HAp were discussed on. Figure 7 and 8 shows calculated phonon dispersion curves of pure HAp with GGA and LDA, respectively. Phonon dispersion curves were composed of some blocks. Experimentally, phonon modes of HAp were assigned by isolated molecular group. Table 3 summarized calculated and experimental frequencies with assignment to isolated molecular group. Present calculations reasonably reproduced experimental value while LDA tended to underestimate frequencies and GGA tended to overestimate them. These are the general tendencies of LDA and GGA. Calderín et al. indicated that some modes were not simply represented by these assignments [31]. In the present calculations, eigenvectors of phonon had same feature that they reported. For example, in GGA-PBE calculations, E_1 mode of 1030 cm^{-1} was composed of OH^- libration and PO_4^{3-} ν_3 modes and A mode of 986 cm^{-1} was based on ν_3 mode of PO_4^{3-}, but one oxygen atom did not move.

Thermal properties of pure HAp were shown in figure 9 and 10. These calculations reasonably agreed with experiment. Calculated specific heats were smaller that experimental one. Two reasons were considered. Calculated specific heats were at constant volume while that of experiment was at constant pressure. Thermo dynamical relation between *Cv* and *Cp* were given by $Cp - Cv = \alpha^2 VBT$, where α was linear thermal expansion coefficient, *V* was volume, *B* was bulk modulus and *T* was temperature. This formula represented that *Cp* was larger than *Cv* at high temperature. On the other hand, phonon calculations were carried out under harmonic approximation in this study. Thus, the effects of anharmonic term such as thermal expansion were not included in the present calculations. Generally,

the effect of anhamonic term was strong at high temperature. Thus, it might be possible for anharmonic term to affect to specific heat.

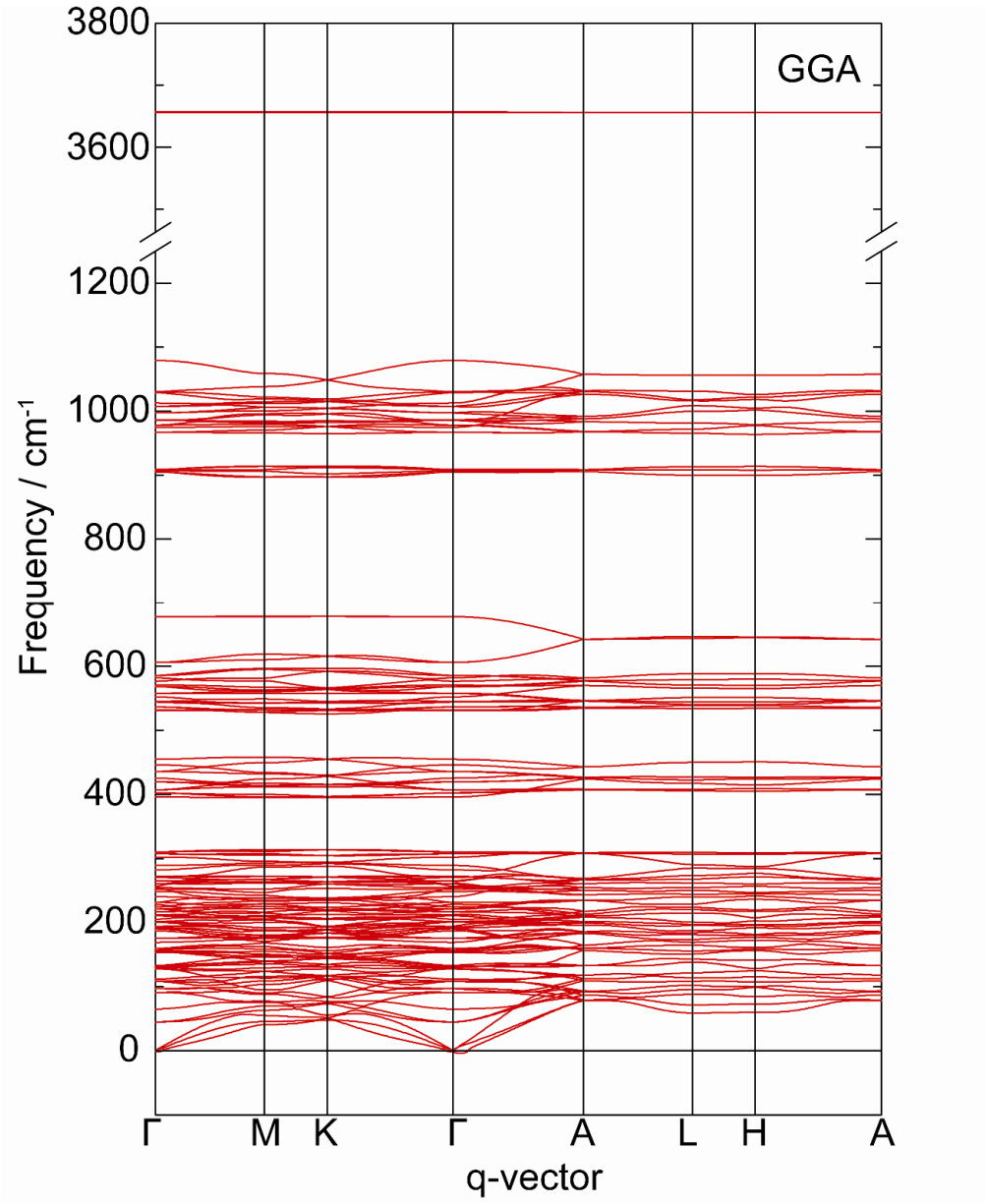

Figure 7 Phonon dispersion curves of pure HAp calculated by GGA-PBE.

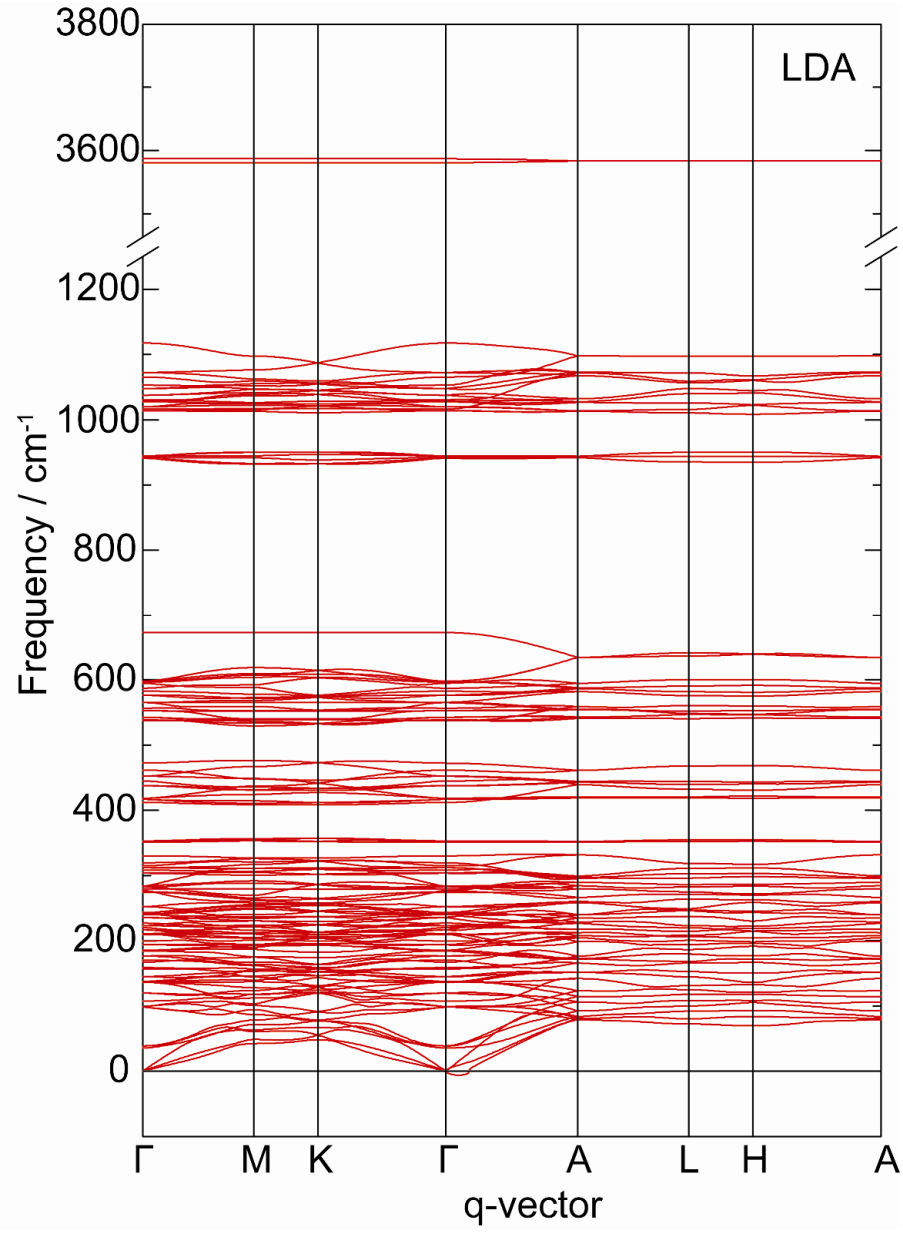

Figure 8 Phonon dispersion curves of pure HAp calculated by LDA.

Table 3 Calculated and experimental frequencies of IR active modes.

PBE		LDA		Expt.[a]
Frequency / cm^{-1}	mode	Frequency / cm^{-1}	mode	Frequency / cm^{-1}
OH stretching				
3655	A	3581	A	3572
PO_4 ν_3				
1030	E_1	1072	E_1	1087
1029	A	1066	A	1072
986	E_1	1031	A	1046
986	A	1028	E_1	1032
978	E_1	1020	E_1	
975	A	1016	A	
PO_4 ν_1				
907	E_1	942	E_1	962
906	A	942	A	
OH libration				
606	E_1	598	E_1	630
PO_4 ν_4				
568	E_1	587	A	601
558	E_1	577	E_1	571

[a] reference 29

Table 3 (continued)

GGA-PBE		LDA		Expt.[a]
Frequency / cm^{-1}	mode	Frequency / cm^{-1}	mode	Frequency / cm^{-1}
537	E_1	566	A	
577	A	565	E_1	
552	A	543	E_1	
		PO_4 ν_2		
436	E_1	537	A	474
403	E_1	462	A	462
531	A	452	E_1	
446	A	445	A	
426	A	417	E_1	
		Ca_3-OH		
310	E_1	353	E_1	355
				343
		lattice mode		
282	A	315	A	290
272	E_1	312	E_1	275
271	A	308	A	228
257	A	284	E_1	n/a

[a] reference 29

Table 3 (continued)

GGA-PBE		LDA		Expt.[a]
Frequency / cm^{-1}	mode	Frequency / cm^{-1}	mode	Frequency / cm^{-1}
254	E_1	277	A	n/a
240	A	275	A	n/a
221	E_1	241	E_1	n/a
212	E_1	236	E_1	n/a
205	A	223	E_1	n/a
201	A	220	A	n/a
201	E_1	209	A	n/a
176	E_1	194	E_1	n/a
169	A	185	A	n/a
159	E_1	184	E_1	n/a
154	A	170	A	n/a
132	A	157	A	n/a
130	E_1	136	E_1	n/a
109	A	108	A	n/a
91	E_1	98	E_1	n/a
45	E_1	39	E_1	n/a

[a] reference 29

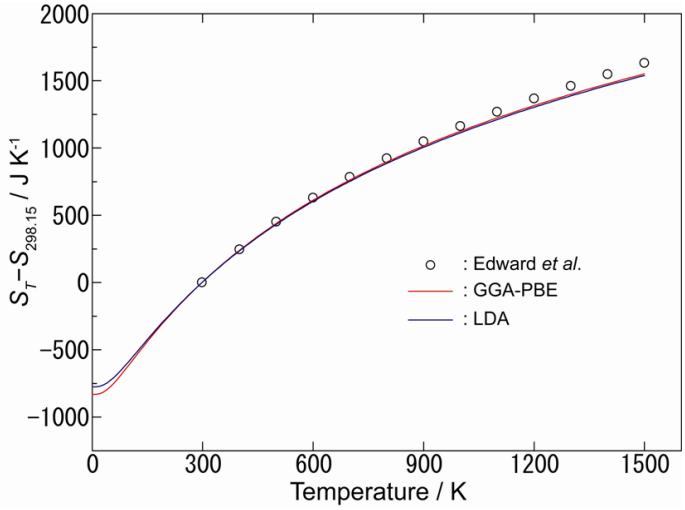

Figure 9 Calculated and experimental entropy of pure HAp.

Experimental data was by Edward et al. [32].

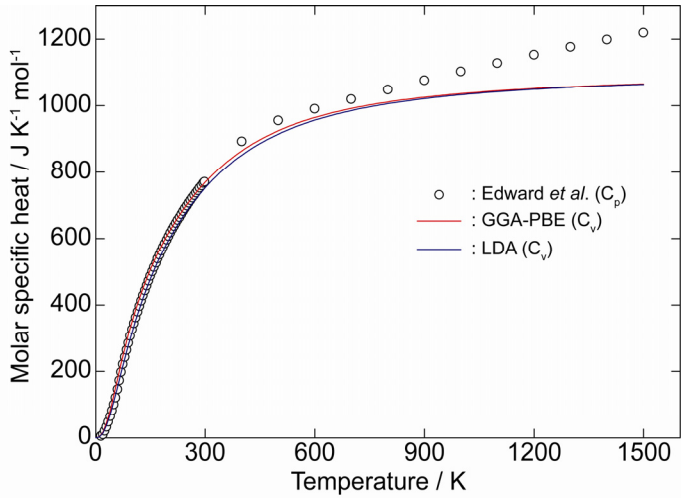

Figure 10 Molar specific heat of pure HAp.

It is noted that calculated specific heat is volume-constant specific heat *Cv*, and that of experiment is pressure-constant specific heat *Cp*. Experimental data was by Edward et al. [32]

Lattice dynamics of Sr^{2+}-doped HAp

Figure 11 and 12 shows phonon DOS of pure and Sr^{2+}-doped HAp. They have similar feature except that some modes were split, such as OH^- libration mode around 600 cm^{-1} and OH^- stretching mode around 3600 cm^{-1}. These changes were derived from local structural distortion caused by Sr^{2+}-doping. It was noted that imaginary modes were appeared in some models. These might be result from small supercell size. DOS of these imaginary modes were rather small and neglected in this study. It was mentioned that the effect of cell relaxations to phonon DOS were small shift to low frequency, as shown in figure 11 and 12. Generally, volume expansion was the origin of shift to low frequency. Sr^{2+}-doping caused volume expansion as discussed above and thus phonon DOS was shifted to low frequency.

Experimentally, lattice dynamics of Sr^{2+}-doped HAp were investigated with infrared and Raman spectroscopies. Sr^{2+} doping into HAp resulted in peak shifts and broadenings of OH^- modes while new peaks induced by Sr^{2+} doping were not reported. In the present calculations, these changes could be explained. As discussed above, lattice expansion caused by Sr^{2+} doping lead to the shifts. These shifts had similar tendencies to experiments. On the other hand, the calculations of OH^- modes showed the splitting of the peaks depending on the distortion around OH^- caused by Sr^{2+}. Thus, various kinds of OH^- modes would be measured. This is because the peaks of OH^- were broadened.

In order to investigate vibrational states of Sr^{2+}, figure 13 and figure 14 shows partial phonon DOS of Sr^{2+}. Compared with partial phonon DOS of Ca^{2+}, DOS of Sr^{2+} had lower frequencies than those of Ca^{2+}. This is because Sr^{2+} has heavier than Ca^{2+}. Partial phonon DOS of Sr^{2+} have somehow similar feature

regardless of different substation site, in that peak of DOS was around 250 cm^{-1}. Thus, the contribution to free energy of Sr^{2+} itself might be similar. Eigenvectors of the modes that Sr^{2+} was related were carefully investigated. These modes were not composed of Sr^{2+} only but also contained the contribution of surrounding atoms. In other words, Sr^{2+}-doping affected the vibrational states of surrounding atoms. To analyze the effect of Sr^{2+}-doping to surrounding atoms, figure 15 shows differences of integral phonon DOS between substitution sites of Sr^{2+}. Below 200 cm^{-1}, Sr^{2+} substituted for Ca-2 site had more states than Sr^{2+} substituted for Ca-1 site. As discussed above, the contribution of temperature dependence of free energy was remarkable for low frequency mode. Therefore, it was expected that the contribution of phonon stabilize Sr^{2+} substituted for Ca-2 site.

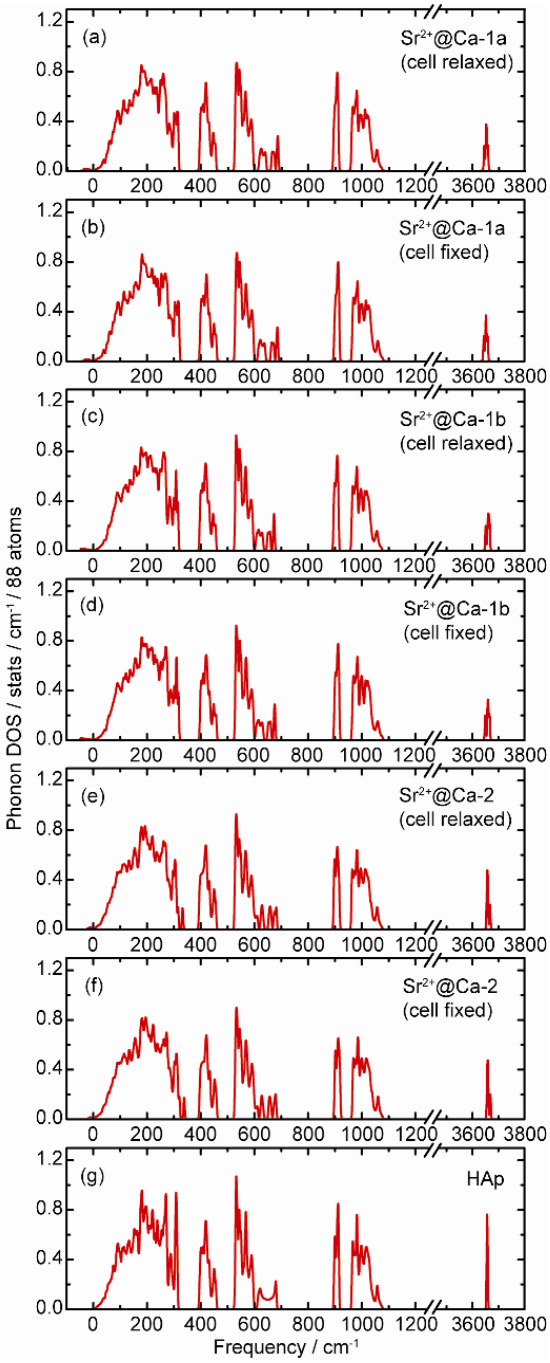

Figure 11 Phonon DOS of Sr^{2+}-doped HAp and pure HAp calculated by GGA. Sr^{2+} substituted for Ca-1a site in (a) cell relaxed model and (b) cell fixed model, Ca-1b site in (c) cell relaxed model and (d) cell, Ca-2 site in (e) cell relaxed model and (f) cell and (g) pure HAp

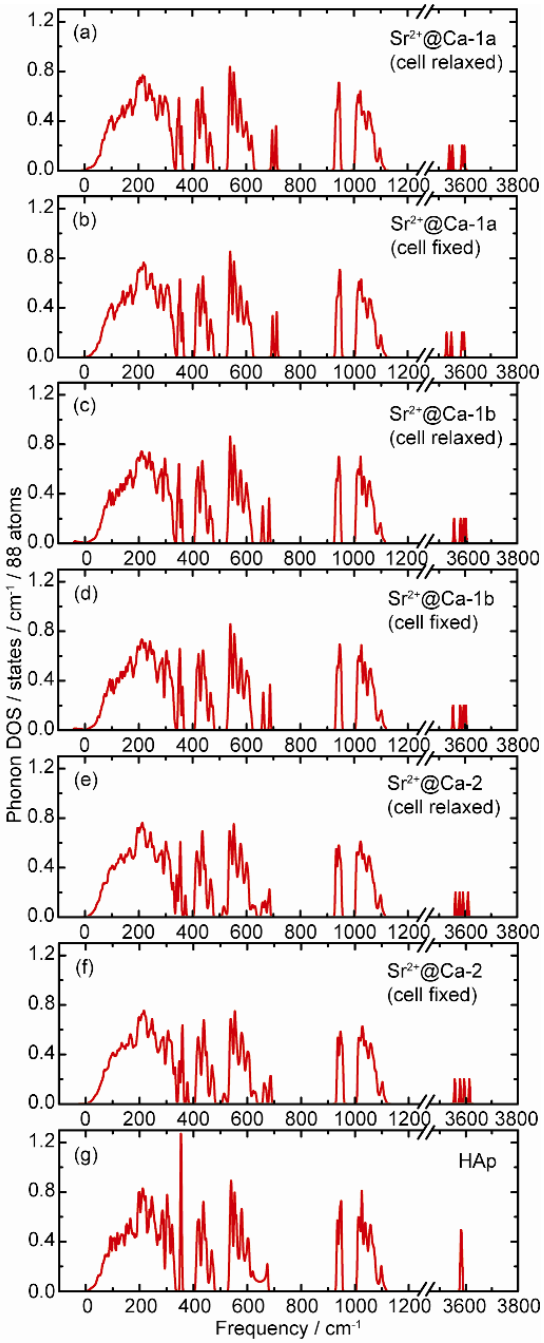

Figure 12 Phonon DOS of Sr^{2+}-doped HAp and pure HAp calculated by LDA. Sr^{2+} substituted for Ca-1a site in (a) cell relaxed model and (b) cell fixed model, Ca-1b site in (c) cell relaxed model and (d) cell, Ca-2 site in (e) cell relaxed model and (f) cell and (g) pure HAp

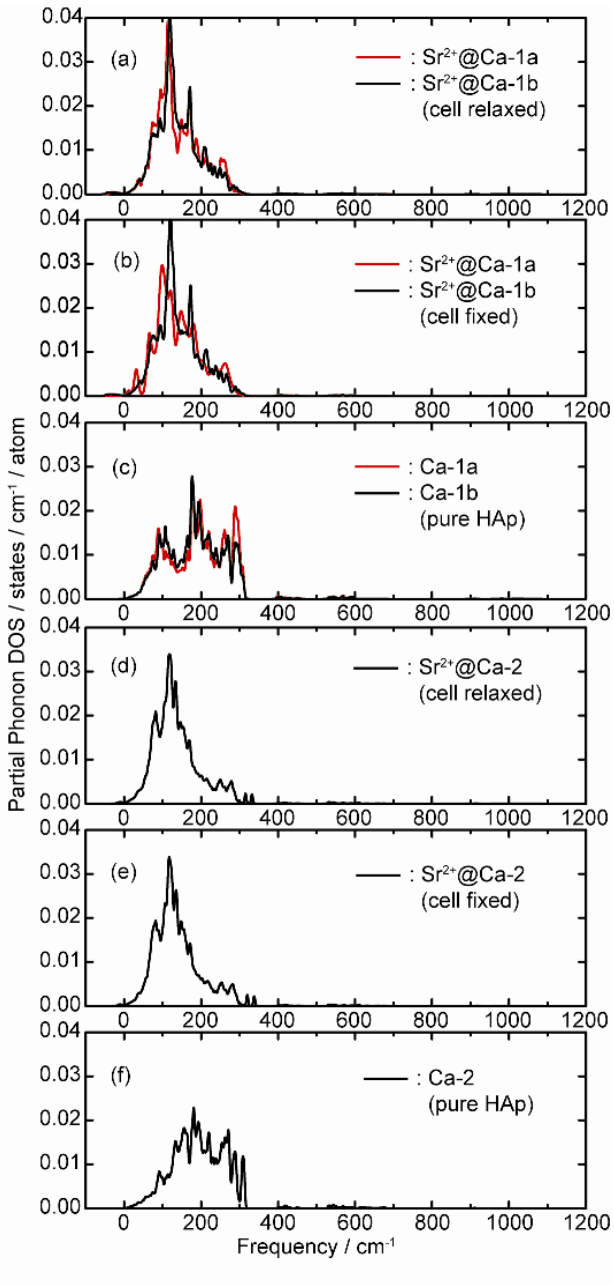

Figure 13 Partial phonon DOS of Sr^{2+} and Ca^{2+} calculated by LDA.

(a) Sr^{2+} substituted for Ca-1 site in cell relaxed model and (b) cell fixed model, Ca-1 of pure HAp, (d) Sr^{2+} substituted for Ca-2 site in cell relaxed model and (e) cell fixed model and Ca-2 of pure HAp

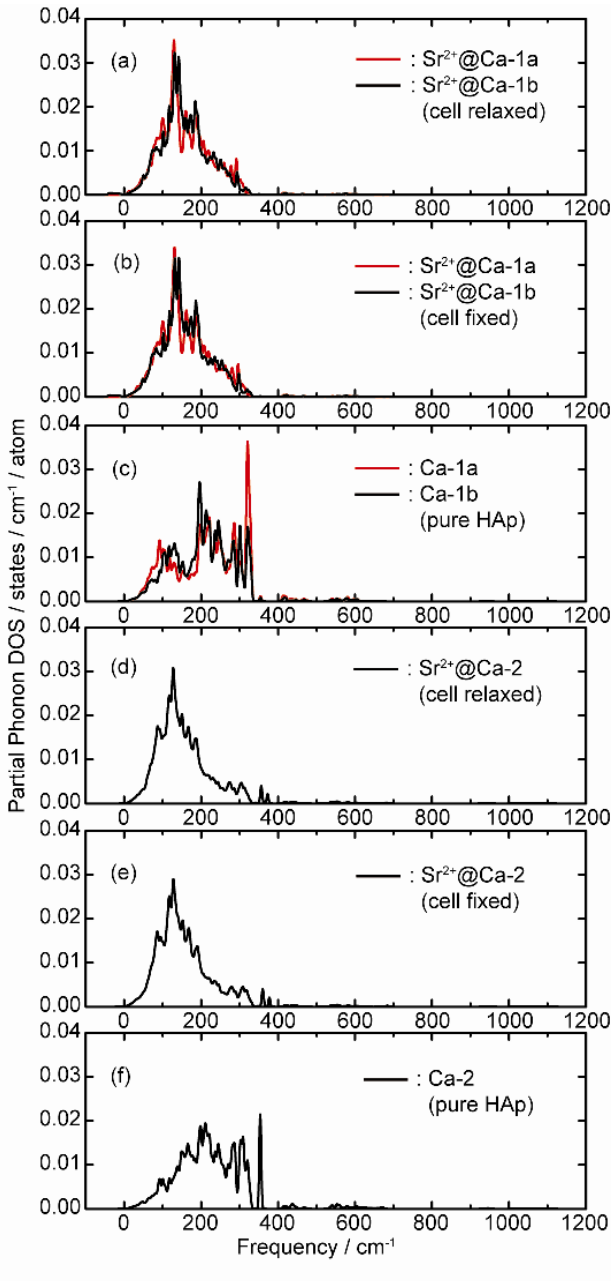

Figure 14 Partial phonon DOS of Sr^{2+} and Ca^{2+} calculated by LDA.

(a) Sr^{2+} substituted for Ca-1 site in cell relaxed model and (b) cell fixed model, Ca-1 of pure HAp, (d) Sr^{2+} substituted for Ca-2 site in cell relaxed model and (e) cell fixed model and Ca-2 of pure HAp

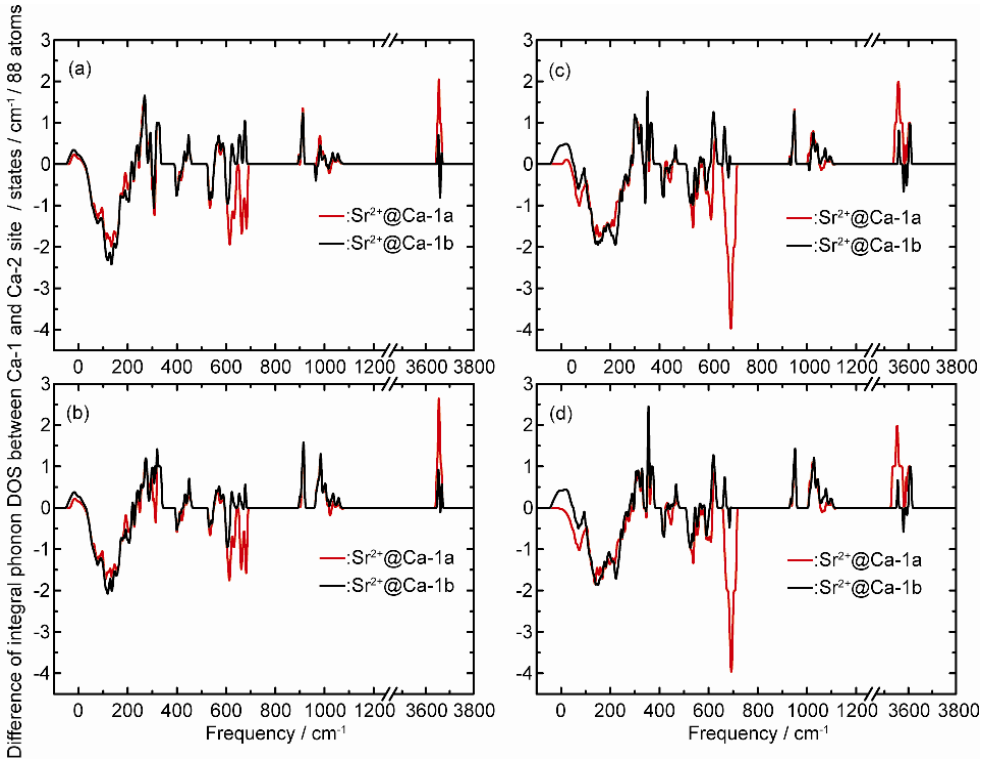

Figure 15 Difference of integral phonon DOS of Sr^{2+}-doped HAp between Ca-1 and Ca-2 site. (a) cell relaxed and (b) cell fixed model calculated with GGA-PBE and (c) cell relaxed and (d) cell fixed model calculated with LDA. Plus number means that integral phonon DOS of Sr^{2+} substituted for Ca-1 site was larger than that of Sr^{2+} substituted for Ca-2 site.

Thermal properties and site preference of Sr^{2+}-doped HAp

Relative free energies between Sr^{2+} substituted for Ca-1 and Ca-2 site were defined as $\Delta F = F_{Sr^{2+}@Ca-1} - F_{Sr^{2+}@Ca-2}$. Difference of vibrational free energies of Sr^{2+}-doped HAp and configuration entropy term $-TS_{config}$ were shown in figure 16 and 17, respectively. Sr^{2+} substituted for Ca-2 site has lower vibrational free energy than those of Ca-1 site. It was noted that difference of free energy between Sr^{2+}-substituted for Ca-1 and Ca-2 site were larger than configuration entropy term. Therefore, vibrational free energy stabilized Ca-2 site.

Figure 18 shows temperature dependence of relative Helmholtz free energy of Sr^{2+}-doped HAp. At ground state, Sr^{2+} prefers Ca-1 site to Ca-2 site even if zero point energies were included. As temperature increase, Sr^{2+} substituted for Ca-2 site was stabilized and finally, Sr^{2+} prefers Ca-2 site. As discussed above, difference of the vibrational free energies were larger than difference of the configuration entropy term. Therefore, the major factor of the stabilization of Sr^{2+} substituted for Ca-2 site was the contribution of phonon.

Figure 19 shows site occupancy ratio of Sr^{2+} in HAp, evaluated from difference of free energy. At ground states, 0 K, Ca-1 site were preferential site and there were few Sr^{2+} substituted for Ca-2 site. As temperature increase, amount of Sr^{2+} substituted for Ca-2 site were increase. Finally, preferential substitution site was change to Ca-2 site. These results were reasonably reproduced experimental results discussed above.

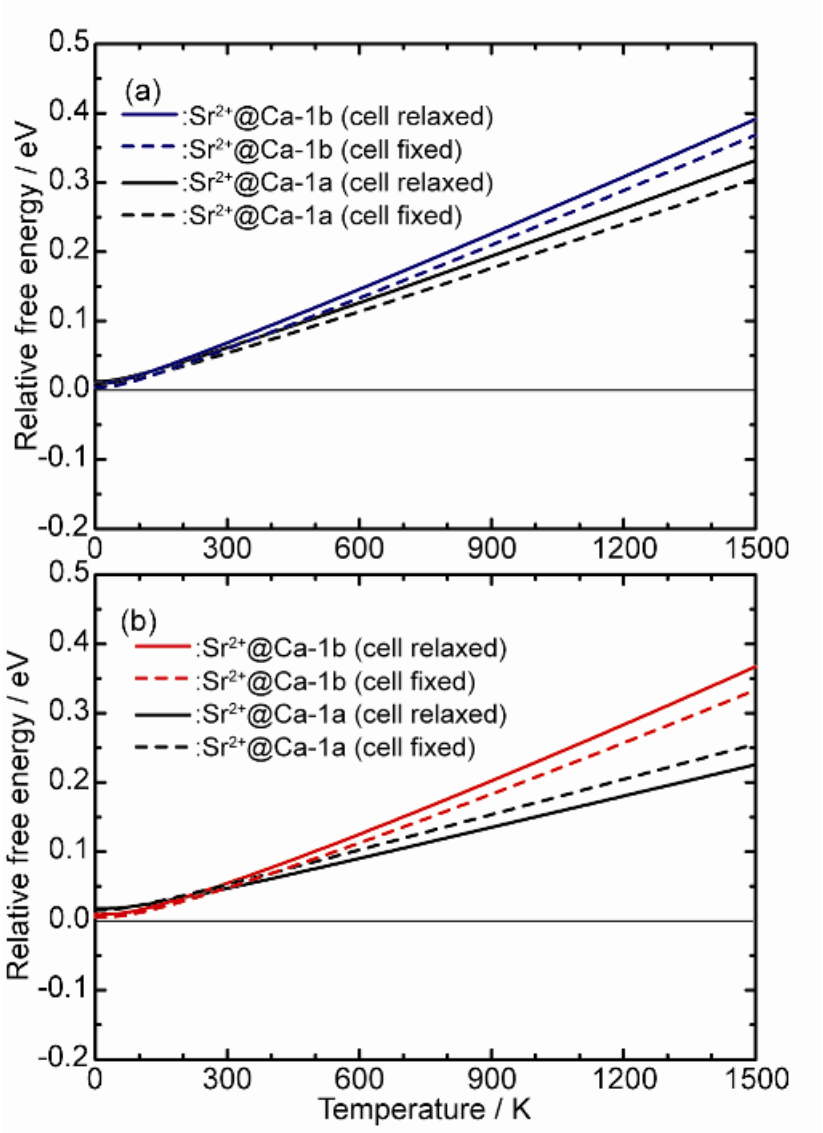

Figure 16 Temperature dependence of relative vibrational free energy based on Sr^{2+} substituted for Ca-2 site. Calculated by (a) GGA-PBE and (b) LDA. Zero was set to free energy of Sr^{2+} substituted for Ca-2 site.

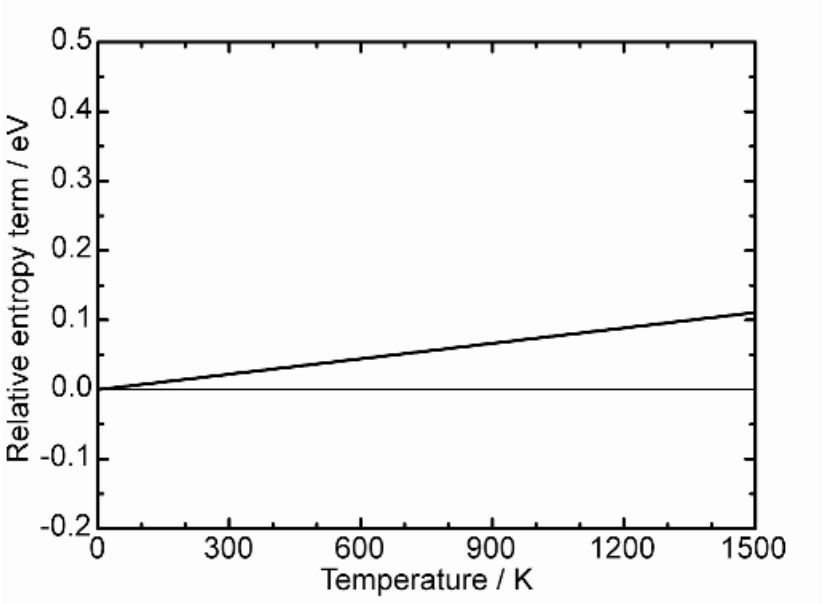

Figure 17 Relative configuration entropy term $-TS_{config}$.

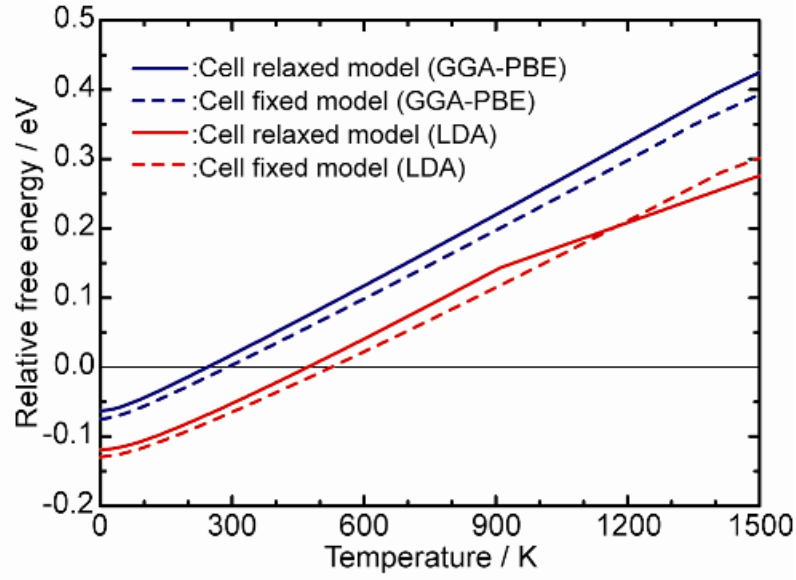

Figure 18 Temperature dependence of relative free energy of Sr^{2+}-doped HAp.

Zero was set to free energy of Sr^{2+} substituted for Ca-2 site.

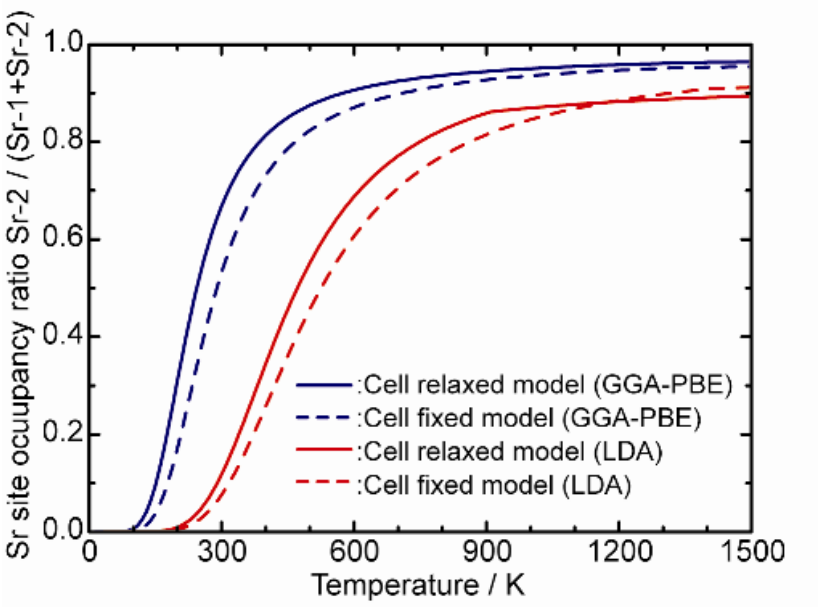

Figure 19 Temperature dependence of ratio of Sr^{2+} substitution site

5. Summary

Temperature effect to Sr^{2+}-doped HAp was experimentally and theoretically investigated.

For experiment, HAp:Sr^{2+} samples were synthesized at different temperature. In this study, the solid-state reaction method and the aqueous precipitation were adopted. Powder XRD measurements indicated that synthesized samples were single phase of HAp:Sr^{2+}. Sr-K XANES indicated that the local environment of Sr^{2+} were different between these samples. Sr-K XANES was analyzed by first-principles supercell method with a core-hole effect. It was found that the amount of Sr^{2+} substituted for Ca-2 site increased at high temperature.

Temperature effects to HAp;Sr^{2+} were analyzed by first-principles lattice dynamics calculations. At ground state, Sr^{2+} substituted for Ca-1 site was more stable than Sr^{2+} substituted for Ca-2 site. Sr^{2+}-doping affect phonon of HAp. The model that Sr^{2+} substituted for Ca-2 site had lower frequencies. Free energy of phonon of Sr^{2+} substituted for Ca-2 site were also lower than Sr^{2+}-substituted for Ca-1 site. It was observed that the preferential site of Sr^{2+} was changed to Ca-2 site at high temperature because of free energy of phonon. This temperature effect could explain the experimental results.

Reference

[1] E. Boanini, M. Gazzano and A. Bigi, Acta Biomater. 6, 1882-1894 (2010).

[2] J. C. Elliott, Structure and Chemistry of the Apatites and Other Calcium Orthophosphates, Amsterdam, Elsevier, (1994).

[3] H. B. Pan, Z. Y. Li, W. M. Lam, J. C. Wong, B. W. Darvell, K. D. K. Luk and W. W. Lu, Biomaterials 5, 1678-1685 (2009).

[4] H. Aoki, S. Okayama, K. Kondo and M. Akao, Biomed. Mater. Eng. 3, 25-31 (1993).

[5] C. Capuccini, P. Torricellii, E. Boanini, M. Gazzano, R. Giardino and A. Bigi, J. Biomed. Mater. Res. 89 A, 594-600 (2009).

[6] M. D. O'Donnell, Y. Fredholm, A. de Rouffignac and R. G. Hill, Acta Biomater 4, 1455-1464 (2008).

[7] K. Zhu, K. Yanagisawa, R. Shimanouchi, A. Onda and K. Kajiyoshi, J. Eur. Ceram. Soc. 26, 509-513 (2006).

[8] J. Terra, E. R. Dourado, J. G. Eon, D. E. Ellis, G. Gonzalezd and A. M. Rossia, Phys. Chem. Chem. Phys. 11, 568-577 (2009)

[9] B. O. Fowler, Inorg. Chem. 13, 207-14 (1974).

[10] K. Matsunaga, H. Inamori and H. Murata, Phys. Rev. B 78, 094101 (2008).

[11] K. Matsunaga and H. Murata, J. Phys. Chem. B 113, 3584-3589 (2009).

[12] K. Matsunaga, J. Am. Ceram. Soc. 93, 1-14 (2010).

[13] K. Kawabata and T. Yamamoto, J. Ceram. Soc. Japan 118, 548-549 (2010).

[14] A. Kuwabara, T. Tohei, T. Yamamoto and I. Tanaka, Phys. Rev. B 71, 064301 (2005).

[15] A. Kuwabara, K. Matsunaga and I. Tanaka, Phys. Rev. B 78, 064104 (2008).

[16] H. Murata, T. Yamamoto and I. Tanaka, Mater. Trans. 50, 999-1003 (2009).

[17] U. D. Wdowik and K. Parlinski, J. Phys.: Condens. Matter 21, 125601 (2009).

[18] P. E. Blochl, Phys. Rev. B 50 17953 (1994).

[19] G. Kresse and J. Furthmuller, Phys. Rev. B 54, 11169 (1996).

[20] G. Kresse and J. Furthmuller, Comput. Mater. Sci. 6 15 (1996).

[21] G. Kresse G and D. Joubert, Phys. Rev. B 59, 1758 (1999).

[22] H. J. Monkhorst and J. D. Pack, Phys. Rev. B 13, 5188 (1976).

[23] J. P. Perdew, K. Burke and M. Ernzerhof, Phys. Rev. Lett. 77, 3865 (1996).

[24] P. Blaha, K. Schwarz, G. Madsen, D. Kvasicka and J. Luitz, WIEN2k, an augmented plane wave + local orbitals program for calculating crystal properties. Techn. Universitat Wien, Austria; ISBN: 3-9501031-1-2 (2001).

[25] I. Tanaka and T. Mizoguchi, J. Phys.: Condens. Matter 21 104201 (2009).

[26] M. I. Kay, R. A. Young and A. S Posner, Nature 204 1050-1052 (1964).

[27] K. Parlinksi, Z. Q. Li and Y. Kawazoe, Phys. Rev. Lett. 78, 4063-4066 (1997).

[28] A. Togo, F. Oba and I. Tanaka, Phys. Rev. B 78, 134106 (2008).

[29] A. S. Posner, A. F. Diorio, Acta Crystallogr. 11, 308-309 (1958).

[30] B. O. Fowler, Inorg. Chem. 13, 194-207 (1974).

[31] L. Calderin, D. Dunfield and M. J. Stott, Phys. Rev. B 72, 224304 (2005).

[32] E. P. Egan Jr, Z. T. Wakefield and K. L. Elmore, J. Am. Chem. Soc. 73, 5579-5580 (1951).

Chapter 5

Summary and Conclusions

In this thesis, electronic and atomic structures of solutes in hydroxyapatite (HAp) were investigated by X-ray absorption near edge structure (XANES) and first-principles calculations. Main points of this thesis were summarized below:

In chapter 2, the local environment of Zn^{2+} in Zn^{2+}-doped Ca^{2+}-deficient hydroxyapatite were investigated by combination of XANES and first-principles calculations. Samples were synthesized by the aqueous-precipitation method. Powder x-ray diffraction (XRD) patterns of these samples were assigned to HAp and no secondary phase was observed. Zn-K XANES spectra were interpreted with first-principles supercell method with a core-hole effect. Simple substitution model that Zn^{2+} was substituted for Ca site in perfect HAp did not reproduce experimental Zn-K XANES. To introduce the effect of Ca^{2+}-deficiency directly, the models that Zn^{2+} was associated with Ca^{2+}-vacancies and excess protons were constructed. Calculated Zn-K XANES of one of these models was in good agreement with experimental one. Therefore, it was concluded that Zn^{2+} was associated with Ca^{2+}-vacancy and excess protons in Ca^{2+}-deficient HAp.

Chapter 3 treated the effects of Ca^{2+}-vacancy to incorporation of solutes, Mg^{2+}, Sr^{2+}, Ba^{2+}, Zn^{2+}, Cd^{2+} and Pb^{2+}, into HAp by first-principles calculations. Calculated models were based on Zn^{2+} in Ca^{2+}-deficient HAp, which was found in chapter 2. Ca^{2+}-vacancy defect complex enables solutes and surrounding atoms to

be further optimized. Optimized models were classified by ionic radii of dopants. On the other hand, electronic structures were depended on the group in the periodic table. Even if local atomic structures resembled each other, electronic structures were different. Defect formation energies of divalent cations in Ca^{2+}-deficient HAp were reduced except Cd^{2+} and Pb^{2+}. These two cations had low substitution energies, and thus, it was useless for them to incorporate into HAp with Ca^{2+}-defect complex. For other cations, the defect formation energies of dopants into Ca^{2+}-deficient HAp were a function of difference of ionic radii between Ca^{2+} and cations. This implied that extra structural relaxation was important factor for decrement of defect formation energies

In Chapter 4, temperature effects to Sr^{2+}-doped HAp were experimentally and theoretically investigated. In experiment, Sr^{2+}-doped HAp samples were synthesized at different temperatures. The XRD profiles of samples were assigned to HAp and no secondary phase was observed. FTIR measurements also showed that samples had typical IR absorption spectra of HAp but they were slightly broad and shifted. Local environments of Sr^{2+} in these samples were investigated by XANES. It was found that Sr^{2+} was substituted for Ca-1 site in the sample synthesized at room temperature. In the sample synthesized at high temperature, the amount of Sr^{2+} substituted for Ca-2 site increased. To analyze these temperature effects, first-principles lattice dynamics calculations of Sr^{2+}-doped HAp were carried out. It was found that effects of phonon stabilized Sr^{2+} substituted for Ca-2 site at high temperature. Composition of Sr^{2+} substituted for Ca-2 site were reasonably reproduced by present calculations.

According to the result of this thesis, it was demonstrated that Ca^{2+}-deficiency and temperature were important factors for solutes to incorporate into HAp. It is useful for these results to control solutes in HAp precisely. We expect that the result of this thesis will lead high-efficiency materials design for HAp-based biomaterials in the near future.

Acknowledgements

The author would like to express his deepest gratitude to Professor Isao Tanaka at Kyoto University for continuous guidance and encouragement throughout this work. The author wishes to express his gratitude to Associate Professor Katsuyuki Matsunaga for helpful discussions and advice. He would like to thank Associate Professor Fumiyasu Oba for his continuous helpful discussions and advices throughout this work. The author wishes to express his gratitude to The author would like to express his deepest gratitude to Professor Jun Kawai and Hiroyuki Nakamura for their critical reading of this thesis.

The author would like to express his gratitude to Professor Atsushi Nakahira for his helpful discussion of preparation of HAp. The author would like to express his gratitude to Associate Professor Teruyasu Mizoguchi at Tokyo University for his helpful discussion of theoretical calculations of Zn-K XANES. The author would like to express his gratitude to Associate Professor Chiya Numako at Tokushima University for her helpful discussion of XAFS.

The author acknowledges Dr. Tomoya Uruga and Dr. Kazuo Kato at JASRI and Dr. Hajime Tanida at Kyoto University for helpful advice and managements on operating at BL01B1 in SPring-8.

The author would like to express his gratitude to Professor Tomoyuki Yamamoto and Professor Akihiko Kitada at Waseda University for wide range of their helpful discussion and encouraged him to enter Ph. D course at Kyoto University to start the research program as shown in this thesis.

The author would like to thank to Dr. Hirofumi Akamatsu and Dr. Hiroyuki Hayashi for his helpful discussion of wide range of experiment. The

author would like to thank to Dr. Atsushi Togo for his helpful discussion of phonon calculations. The author would like to thank to Dr. Yu Kumagai for his helpful discussion of first-principles calculations.

The author would like to thank to Mr. Choi Minseok, Mr. Akifumi Matsumoto and Mr. Yuji Takahashi for giving continuous encouragements. The author wished to make grateful acknowledgement to the members of Professor Tanaka's group for helpful discussions throughout this work.

Finally, the author would like to sincerely than his family for their enduring support and encouragement.